CRYSTALLIZATION AND MELT BEHAVIOR OF *i*-PP AND *i*-PP/GRAPHENE NANOCOMPOSITES

BY

Abdullah Khaleel Ahmed

A Thesis Presented to the
DEANSHIP OF GRADUATE STUDIES

KING FAHD UNIVERSITY OF PETROLEUM & MINERALS
DHAHRAN, SAUDI ARABIA

In Partial Fulfillment of the
Requirements for the Degree of

MASTER OF SCIENCE

In

CHEMICAL ENGINEERING

May 2017

KING FAHD UNIVERSITY OF PETROLEUM & MINERALS
DHAHRAN- 31261, SAUDI ARABIA
DEANSHIP OF GRADUATE STUDIES

This thesis, written by **Abdullah Khaleel Ahmed** under the direction his thesis advisor and approved by his thesis committee, has been presented and accepted by the Dean of Graduate Studies, in partial fulfillment of the requirements for the degree of **MASTER OF SCIENCE IN CHEMICAL ENGINEERING.**

Dr. Mohammed Ba-Shammakh
Department Chairman

Dr. Salam A. Zummo
Dean of Graduate Studies

31/5/17
Date

Dr. Mamdouh Al-Harthi
(Advisor)

Atiqullah
Dr. Muhammad Atiqullah
(Co-Advisor)

Mozahar Hossain
Dr. M. Mozahar Hossain
(Member)

Shaikh Abdur Razzak
Dr. Shaikh Abdur Razzak
(Member)

Dr. Isam Al-Jundi
(Member)

Dedicated to

My Mother, Shakeela Bano

Father, Khaleel Ahmed

Brother, Sisters

Teachers

and

Friends

ACKNOWLEDGMENTS

My greatest gratitude is due to Almighty Allah who gave me strength in each step of this thesis with His endless bounties and blessings.

I thank my thesis advisor Professor Dr. Mamdouh Al-Harthi for his continuous guidance, support, and assistance throughout this work. My special thanks are to Dr. Muhammad Atiqullah (Center for Refining & Petrochemicals, Research Institute), my thesis co-advisor for his meticulous guidance particularly in new and insightful interpretations of results, invaluable advices, continuous encouragement and immense time devoted to train me. I also thank my committee members: Dr. Muhammad Mozahar Hossain, Dr. Shaikh Abdurrazak, and Dr. Issam Al-Jundi for their contributions.

I greatly acknowledge the scholarship provided by King Fahd University of Petroleum & Minerals for pursuing an MS in the Department of Chemical Engineering. The technical assistance provided by the Department of Chemical Engineering and the Center for Refining & Petrochemicals (CRP) at KFUPM, Dhahran, Saudi Arabia is also gratefully acknowledged. I also thank Mr. Sarath P. Unnikari and Mr. Anwar Hossaen for their support in the experimental work. The gift of the polypropylene sample by National Industrialization Company (Tasnee) and support in NMR work by SABIC are thankfully appreciated.

My sincere thanks are forwarded to my most beloved mother Shakeela Bano, my father Khaleel Ahmed, my sisters Mahroz and Sana, and brother Abdurrahman for their love, prayers, support, encouragement, and their invaluable help.

TABLE OF CONTENTS

LIST OF TABLES

LIST OF FIGURES

ABSTRACT

Full name: Abdullah Khaleel Ahmed

Thesis title: Crystallization and Melt Behavior of *i*-PP and *i*-PP/Graphene Nanocomposites

Major field: Chemical Engineering

Date of degree: May 2017

Crystallization and melting are integral parts of isotactic polypropylene (*i*-PP) and *i*-PP/graphene nanocomposites end-product fabrication process. Therefore, the nonisothermal crystallization kinetics and melting behavior of an un-nucleated commercial *i*-PP and nanocomposites of *i*-PP with graphene have been pursued by integrating a new nonisothermal crystallization model, Flory's thermodynamic equilibrium theory, Gibbs-Thompson equation, and DSC experiments. By applying this simple conceptual integration, the relative crystallinity α, temperature-dependent instantaneous crystallinity χ, the crystallization kinetic triplet, and the lamellar thickness distribution have been duly correlated, as appropriate, to the level of undercooling θ, crystal surface free energy D, and critical stable crystallite sequence number n^*. Consequently, new insightful results, interpretations, and explanations have been concluded.

The nonisothermal primary and secondary crystallizations of *i*-PP occur isokinetically with constant (temperature-, entropy-, and cooling rate-invariant) apparent kinetic energy E_a, which is also unaffected by θ, D, and the lamella-inclusive pendant –CH_3 group of the propylene repeat unit. The crystal dimension n_d varies, irrespective of θ and D, from cylinder to sphere, depending on the system entropic disorder. Instantaneous

(athermal/heterogeneous) and sporadic (thermal/homogeneous) nucleation processes may co-prevail.

For *i*-PP/graphene nanocomposites, the roles played by graphene have been especially highlighted that greatly exceed what is currently available in the literature. The occurrence of lamellar thickening with increasing melting temperature (for *i*-PP and *i*-PP/graphene nanocomposites) has been discussed, considering the *chain sliding diffusion theory* proposed by Hikosaka et al., and the variation of θ and D. The present approach applies, in general, to evaluate the influence of catalyst structure, backbone defect types, and their distribution on the crystallization and melt behaviors of polyolefins and polyolefin/nanofiller composites.

ملخص الرسالة

الاسم الكامل: عبدالله خليل أحمد

عنوان الرسالة: تبلور وذوبان سلوك *i*-PP و*i*-PP /الجرافين نانوكومبوسيتس

التخصص: هندسة كيميائية

تاريخ الدرجة العلمية: **١٢ شعبان, ١٤٣٨**

التبلور والذوبان أجزاء لا تتجزأ من البولي بروبلين إيزوتاكتي *i*-PP و*i*-PP /الجرافين نانوكومبوسيتس عملية تصنيع المنتج النهائي. وبناءاً على ذلك، تم اتباع حركية التبلور غير متساوي الحرارة وسلوك الذوبان من دون نواة التجارية *i*-PP و نانوكومبوسيتس من *i*-PP مع الجرافين من خلال دمج نموذج التبلور غير الحرارية الجديدة، نظرية التوازن الحراري لفلوري، ومعادلة جيبس-طومسون، وتجارب DSC. من خلال تطبيق هذاالمفهوم التكاملي البسيط، فإن التبلور النسبي α، التبلور اللحظي الذي يعتمد على درجة الحرارة χ، التبلور ثلاثي الحركة، وتوزيع سمك الصفائح كان مرتبطاً حسب الأصول، حسب الاقتضاء، بمستوى التشبع السفلي θ، ومستقر عدد تسلسل مستقر البلورات * n . ونتيجة لذلك، تم التوصل إلى نتائج ثاقبة، وتفسيرات، وتوضيحات جديدة.

التبلور الابتدائي والثانوي غير متساوي الحرارية ل*i*-PP تحدث إيزوكينتيكالي مع ثابت (درجة الحرارة، والانتروبي، والتبريد معدل ثابت) الطاقة الحركية الظاهرية E_a، والتي لا تتأثر أيضاً ب θ وD ومجموعة قلادة لاميلا شاملة CH_3– المجموعة من وحدة تكرار البروبيلين. يختلف البعد البلوري، بغض النظر عن θ و D، من الاسطوانة إلى المجال، اعتماداً على اضطراب النظام الانتروبي. ويمكن أن تسود العمليات التنموية لحظية (حرارية / غير متجانسة) وعمليات متفرقة (حرارية / متجانسة).

بالنسبة للمركبات النانوية من الجرافين *i*-PP/الجرافين، تم تسليط الضوء على الأدوار التي لعبها الجرافين بشكل خاص والتي تتجاوز كثيراً ما هو متاح حالياً في المراجع. وقد نوقش حدوث سماكة صفائحية مع زيادة درجة حرارة

الانصهار(ل*i*-PP و*i*-PP /الجرافين نانوكومبوسيتس)،مع الأخذ بعين الأعتبار *نظرية أنتشار انزلاق السلسلة* المقترحة من قبل هيكوساكا وآخرون، والاختلاف ل θ وD. النهج الحالي ينطبق، بشكل عام، لتقييم تأثير هيكل الحفاز، وأنواع عظم العمود الفقري، وتوزيعها على تصرف التبلور والأنصهار لمركبات البولي أوليفين والبولي أوليفين / حشونانو.

CHAPTER 1

INTRODUCTION

1.1 Propylene

Propylene commonly known as propene is an unsaturated organic compound with chemical formula C_3H_6. The structure of propylene is shown in Figure 1. It owns one double bond and after ethylene it is considered as second simplest member of alkene class of hydrocarbons as well as in terms of natural abundance. It is a colorless, low boiling, flammable, highly volatile gas at room temperature. Propylene is basic component in the modern petrochemical and organic synthesis [1].

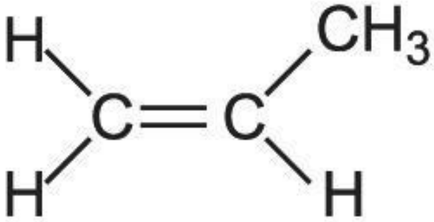

Figure 1: Propylene structure.

Due to higher mass propylene has higher boiling point and density than ethylene. Propylene is considered as one of highest volume chemical products of petrochemical industry. Different routes to produce propylene is presented below in Figure 2 [2].

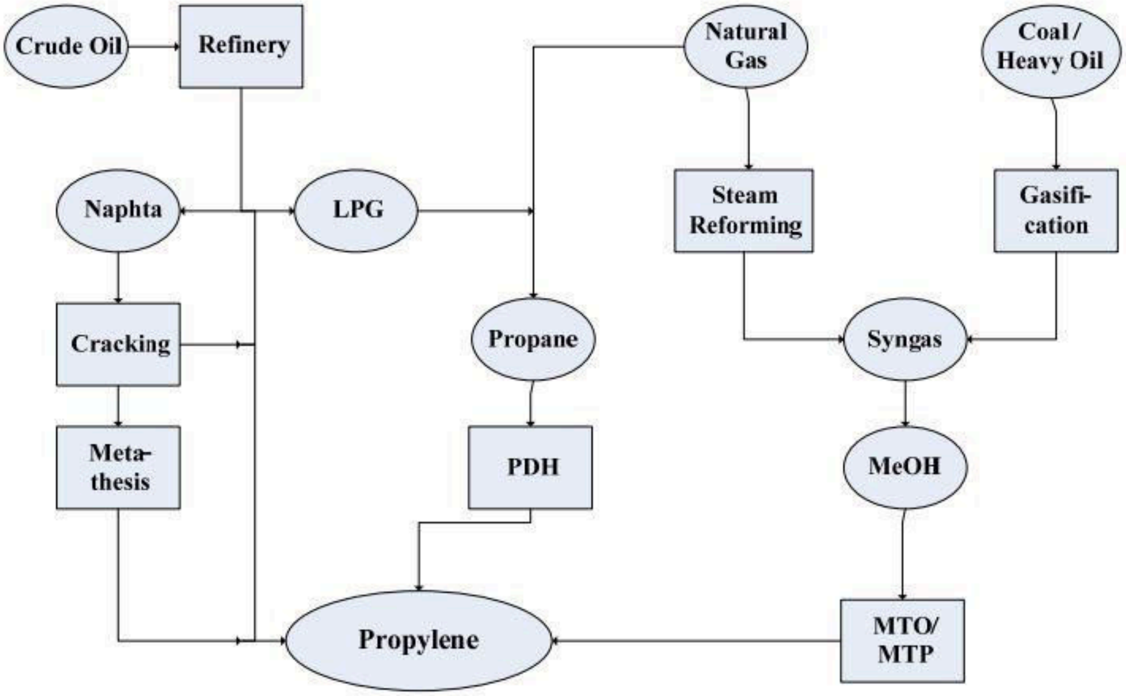

Figure 2: Propylene value chain [2].

Most of worldwide propylene production comes from steam crackers. Fluid catalytic cracking (FCC) units from refineries are second important source of propylene and recently specific on-purpose processes, such as propane dehydrogenation, metathesis and others are getting more and more attention [3].

Propene is used as a chemical intermediate in the production of polypropylene, acrylonitrile, propylene oxide, isopropanol, and cumene. Refineries use much of their production of propene internally as a refinery heating gas, to produce alkylates in gasoline, and to produce liquefied petroleum gas [4].

In 2015, the global demand for propylene, polymer grade (PG) and chemical grade (CG) combined, is estimated at 94.2 million tons. The chart in Figure 3 outlines the propylene global demand profile for 2015.

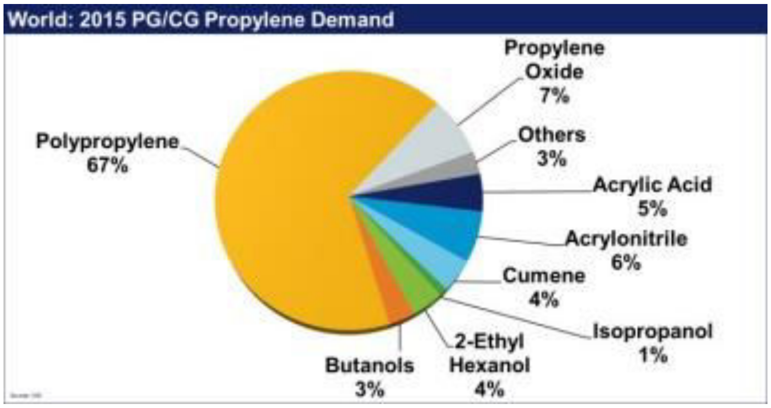

Figure 3: World PG/CG Propylene Demand 2015.

Source URL: https://www.acs.org/content/acs/en/pressroom/cutting-edge-chemistry/the-propylene-quandary.html

In 2015 around 67% of propylene was used in production of polypropylene. Almost 7% of total propylene was used for producing propylene oxide, 5% for acrylic acid, 6% for acrylonitrile, 4% for cumene, 3% for butanol, 4% for 2-ethyl hexanol and remaining for other chemicals.

Top five propylene producing countries are China, USA, South Korea, India and Saudi Arabia (Table 1) which together account for 79% of worlds total production.

Table 1: Top five propylene producing countries.

Country	Propylene production 2014 (Million tons)
China	26.9
USA	5.1
South Korea	2.7
India	2.3
Saudi Arabia	1.6

Source URL: http://irpc.listedcompany.com/misc/PRESN/20150515-propylene-market-analyst.pdf

1.2 Polypropylene types and backbone

For the first time in history polypropylene (PP) (Figure 4) was prepared by Giulio Natta using Ziegler-Natta catalyst in early 1950s and was taken into commercial production in 1957. PP expressed as C_nH_{2n} is a linear hydrocarbon polymer. PP as a thermoplastic polymer resin has applications both in the average household and in industrial and commercial applications. PP, like polyethylene (PE) and polybutene (PB), is a saturated polymer commonly known as polyolefin. The chemical designation is C_3H_6. Also PP is one of those most versatile polymers which can be used both as a fiber and as a plastic, in almost all of the plastics end-use markets. PP offers a good balance of properties and cost unachieved by most thermoplastics.

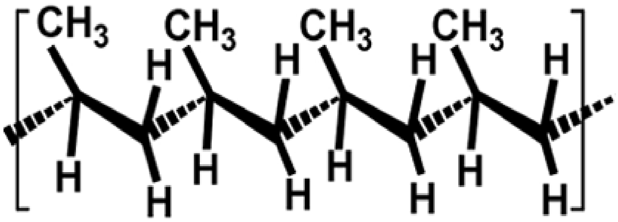

Figure 4: Polypropylene backbone.

Almost all of the commercial PP is isotactic and has crystallinity between low-density polyethylene (LDPE) and high-density polyethylene (HDPE). Copolymerization of PP with ethylene makes it more tough and flexible and makes PP an engineering thermoplastic having properties comparable to material such as acrylonitrile-butadiene-styrene (ABS). PP is economical compared to other polymers and usually pigments are used to make it opaque or colored. Also PP is having good resistance to fatigue. Melting point of PP is usually determined using differential scanning calorimetry. Isotactic polypropylene (*i*-PP) has a melting point that ranges from 160 ºC to 166 °C depending on its crystallinity and composition. Syndiotactic PP is having melting point of 130 °C of 30% crystallinity. The measurement of molecular weight of polymers is expressed as melt flow index (MFI). The measurement of MFI gives information on flow behaviour of molten polymers during processing. Generally PP is divided into three groups: homopolymers, random copolymer, and block copolymer.

1.3 Polypropylene process technology

Polypropylene was produced using Slurry process by early manufacturers. Hexane was used as solvent and diethylaluminuium chloride was best choice as cocatalyst. At the end isotactic PP is precipitated but large amount of atactic portion of PP remains dissolved in Hexane. Because of the reasons like low activity of catalysts, large portion of atactic polymer and the process itself being costly, only few of plants at present are using this technology.

The second process to produce PP is Bulk process. In bulk process polymerization happens in liquid propylene is similar to slurry process in which PP is precipitated as produced. In most of cases of this process, polymerization occurs in continuous stirred tank reactors or autoclaves.

The other important process known as Loop Slurry Process Figure 5 was developed by Chevron Phillips Chemicals in which polymerization is carried out in a jacketed pipe reactor in rapidly circulating liquid propylene. This is process is also called CP Chem process. The difference between Bulk process and CP Chem is the use of vessel. Bulk process mostly uses continuous stirred tanks or autoclaves, while CP Chem process is carried out in series of pipe reactor [5].

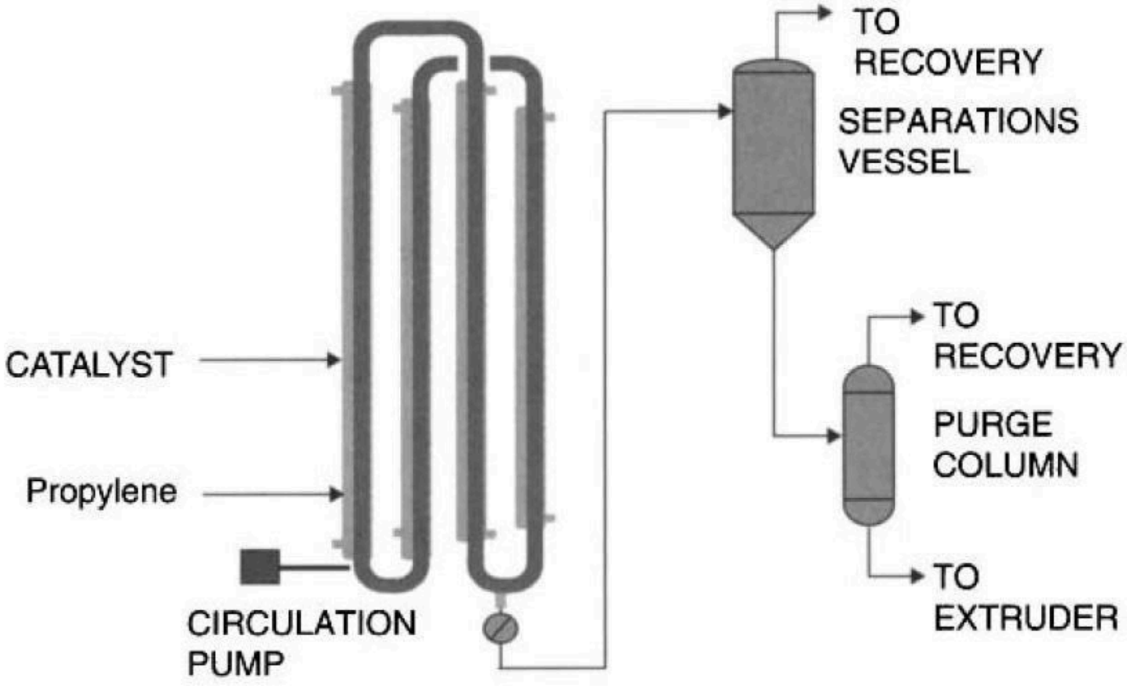

Figure 5: Loop Slurry process [5].

The most important and commonly used process to produce PP is gas phase process. Supported Ziegler Natta catalysts are most widely used and polymerization of propylene occurs in gas phase in virtual absence of solvent.

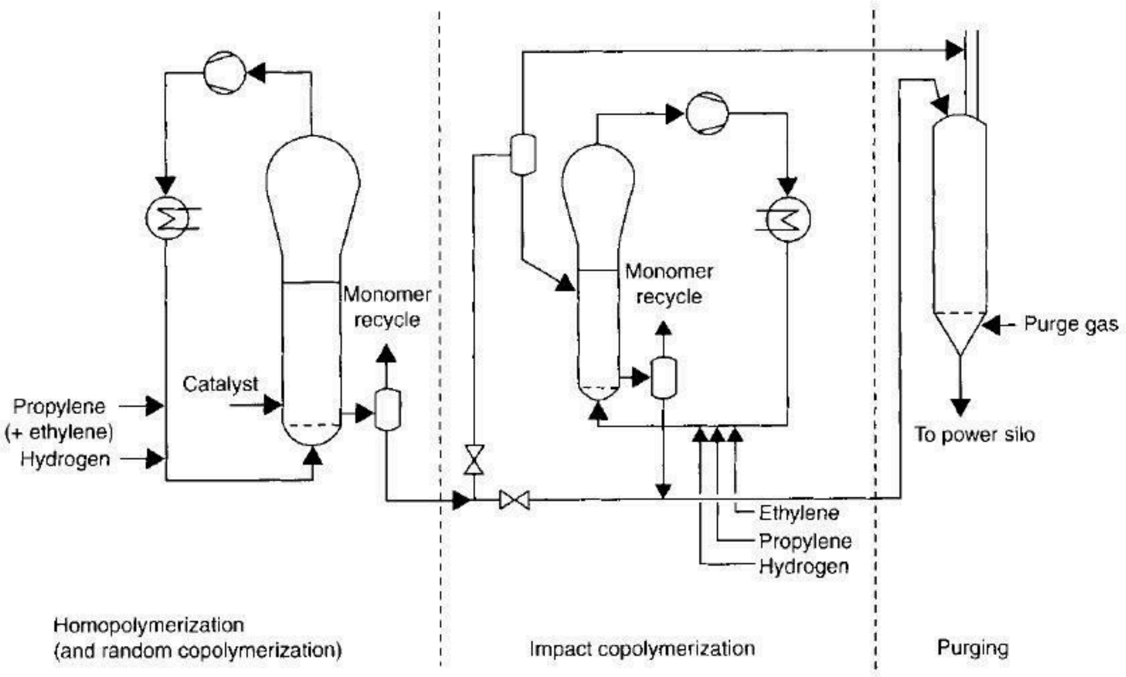

Figure 6: UNIPOL gas phase process [5].

The UNIPOL PP Figure 6 process utilizes a vertical fluidized bed reactor and no mechanical agitation is required. The bulbous upper portion of the reactor has become almost iconic in the polyolefins industry. The bulged part of the reactor is designed to be a particle disengagement zone, allowing suspended particles to fall back into the fluidized bed. It is important to use a catalyst containing a minimum of both very large particles and very fine particles. The former produces large polymer agglomerates that are hard to fluidize, and the latter produces very small polymer particles that are more difficult to disengage from the circulating propylene [5].

1.4 World versus Saudi Arabian polypropylene production volumes

In 2016, the total volume of PP produced globally was approximately 76.81 million metric tons. Top ten producers account for 55% of PP manufactured in the world. The demand for polypropylene has outpaced the other polymers Figure 7. It the highest single polymer produced and used in world alone. Top ten polypropylene producing companies Table 2 account for almost 55% of total polypropylene produced globally. Lyondell Basell, Sinopec Group and PetroChina Group are top three producers respectively in world in 2016. SABIC ranked 6th in world with production of 3.46 million tons.

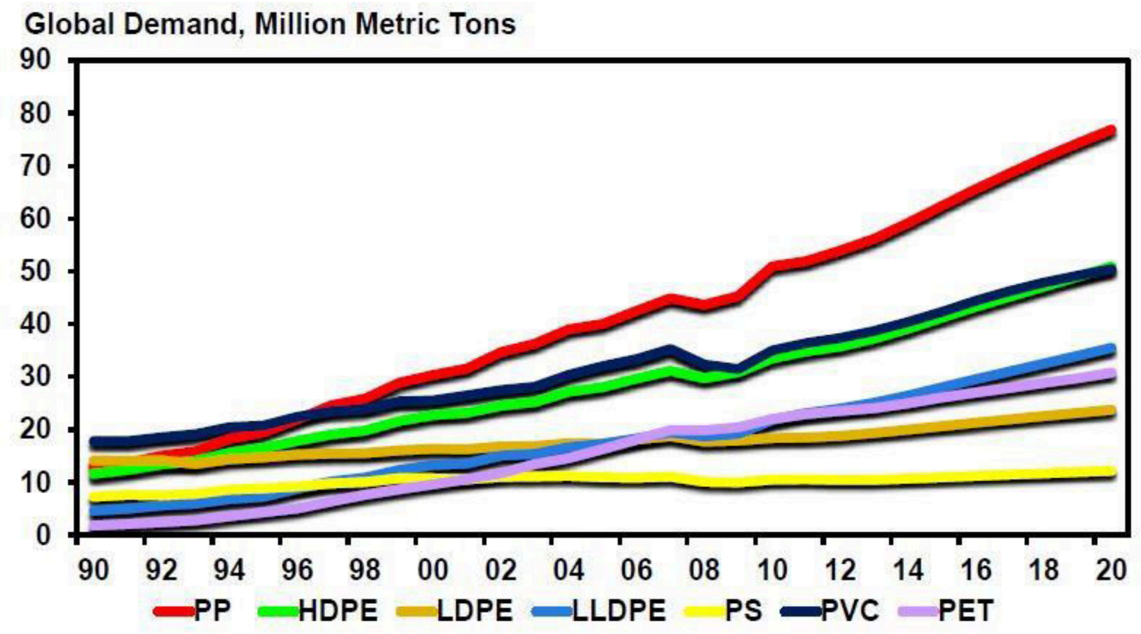

Figure 7: PP growth outpaced other polymers globally.

Source URL: http://www.petrochemconclave.com/presentation/2014/Mr.SMoolji.pdf

Table 2: Top ten polypropylene producing companies in world.

2011	**Capacity (Kt)**	**Rank**	**2016**	**Capacity (Kt)**
Lyondell Basell	6.47	1	Lyondell Basell	6.52
Sinopec Group	4.93	2	Sinopec Group	6.46
Braskem Group	4.03	3	PetroChina Group	4.61
SABIC	3.46	4	Braskem Group	4.03
PetroChina Group	3.04	5	Borealis	3.72
Reliance Industries	2.75	6	SABIC	3.46
Borealis	2.75	7	Exxon Mobil	2.79
Total PC	2.72	8	Reliance Industries	2.75
Exxon Mobil	2.28	9	Total PC	2.72
Formosa Plastic Corp.	2.27	10	Formosa Plastic Corp.	2.27

Source URL: http://www.petrochemconclave.com/presentation/2014/Mr.SMoolji.pdf

1.5 Applications of polypropylene

PP as a thermoplastic polymer resin has applications both in the average household and in industrial and commercial applications. It is one of those most versatile polymers which can be used both as a fiber and as a plastic, in almost all of the plastics end-use markets. An important and growing application of PP is in automotive industry. Compared metal parts, polypropylene makes vehicles light weight keeping them strong which increases fuel efficiency Figure 8 [6].

Figure 8: Lightweight polypropylene from LyondelBasell used in the rear panel of Ford Kuga offered in the European automobile market [6].

Another important application of PP is in packaging. Since glass can be easily broken and has higher density than PP, is being replaced by PP. Specially baby bottles Figure 9 are being made by PP nowadays.

Figure 9: Baby bottles made up of PP [6].

1.6 Ziegler-Natta catalysts for polypropylene

Ziegler-Natta catalysts in general consist of combination of a transition metal compound of an element from group IV to VIII and an organometallic compound with the metal from group I to III of periodic table [7]. Ziegler-Natta catalysts have improved a lot since their discovery in fifties. Catalyst precursors, cocatalysts and internal and external electron donors have been changed with time. Internal donors are related to fraction of stereospecific sites, external donors replace internal donors lost due to reactions and cocatalysts activate catalysts by alkylation and reduction of transition metals [8,9].

Ziegler-Natta catalysts are known in terms of generations according to their development with time. First generation and second generation Ziegler-Natta catalysts are based on crystalline $TiCl_3$. First generation catalyst used to be prepared by reduction of $TiCl_4$. The problem with first generation catalyst was low activity and limited stereoselectivity because of which removal of atactic portion was necessary for propylene polymerization. With time during 1970s Solvay developed improved $TiCl_3$ second generation catalyst. Stereoselectivity of catalyst was improved, atactic was no more problem but still activity was not much [10,11].

Third and fourth generation Ziegler-Natta catalyst consist of $TiCl_4$ supported on porous $MgCl_2$. Third generation catalysts have much better catalyst activity and enhanced isotacticity index compared to second generation catalyst and the fourth generation catalyst is even better than third generation with controlled morphology and better productivity [12,13].

1.7 Catalysts and stereo-defects

Ziegler-Natta catalysts are stereospecific. Isotactic polypropylene is formed when addition of propylene monomers occur in a head to tail manner in same stereo arrangement during polymerization process. During polymerization process any mistake made by stereo irregularities or mis-insertion of propylene monomer i.e. tail-to-tail or head-to-head, is known as a defect. Stereo irregular placement is called stereo defect and mistakes due to wrong insertion results in regio defects [14,15].

Due to presence of an asymmetric carbon, polypropylene has three different stereo configurations termed as isotactic, Syndiotactic and atactic as shown in Figure 10.

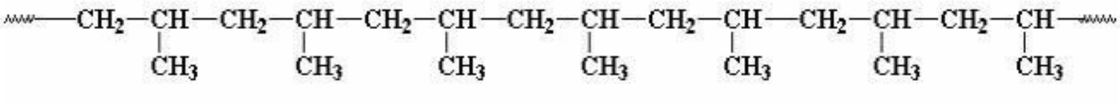

$$\sim CH_2-\underset{CH_3}{\underset{|}{CH}}-CH_2-\underset{CH_3}{\underset{|}{CH}}-CH_2-\underset{CH_3}{\underset{|}{CH}}-CH_2-\underset{CH_3}{\underset{|}{CH}}-CH_2-\underset{CH_3}{\underset{|}{CH}}-CH_2-\underset{CH_3}{\underset{|}{CH}}-CH_2-\underset{CH_3}{\underset{|}{CH}}-\sim$$

Isotactic Polypropylene

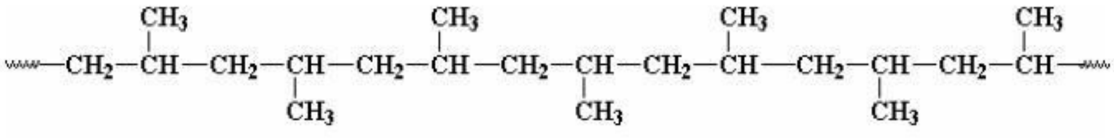

$$\sim CH_2-\overset{CH_3}{\overset{|}{CH}}-CH_2-\underset{CH_3}{\underset{|}{CH}}-CH_2-\overset{CH_3}{\overset{|}{CH}}-CH_2-\underset{CH_3}{\underset{|}{CH}}-CH_2-\overset{CH_3}{\overset{|}{CH}}-CH_2-\underset{CH_3}{\underset{|}{CH}}-CH_2-\overset{CH_3}{\overset{|}{CH}}-\sim$$

Syndiotactic Polypropylene

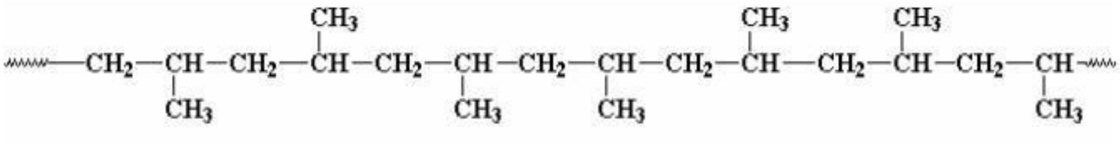

$$\sim CH_2-\underset{CH_3}{\underset{|}{CH}}-CH_2-\overset{CH_3}{\overset{|}{CH}}-CH_2-\underset{CH_3}{\underset{|}{CH}}-CH_2-\underset{CH_3}{\underset{|}{CH}}-CH_2-\overset{CH_3}{\overset{|}{CH}}-CH_2-\overset{CH_3}{\overset{|}{CH}}-CH_2-\underset{CH_3}{\underset{|}{CH}}-\sim$$

Atactic Polypropylene

Figure 10: Different stereo configurations of Polypropylene.

1.8 Graphene

Graphene was first discovered in 2004 when Sir Professor Andrei Geim and co-workers at Manchester University first isolated monolayer samples from highly oriented pyrolytic graphite, using a mechanical cleavage method [16]. The Nobel Prize in physics in 2010 was awarded to Sir Professor Andrei Geim and Sir Professor Kostya Novoselov for their ground breaking experiments regarding graphene. Graphene is a monolayer of carbon atoms packed in a hexagonal lattice as shown in Figure 11. A single layer of graphene is the strongest material existing on earth. With Young's modulus of 1 TPa, ultimate strength of 130 GPa, thermal conductivity 5000 W/m^{2}K, electrical conductivity up to 6000 S/cm and a very high surface area of 2036 m^2/gm makes graphene a wonder material [17–20]. Graphene is the basic building block for graphitic materials of all other dimensionalities

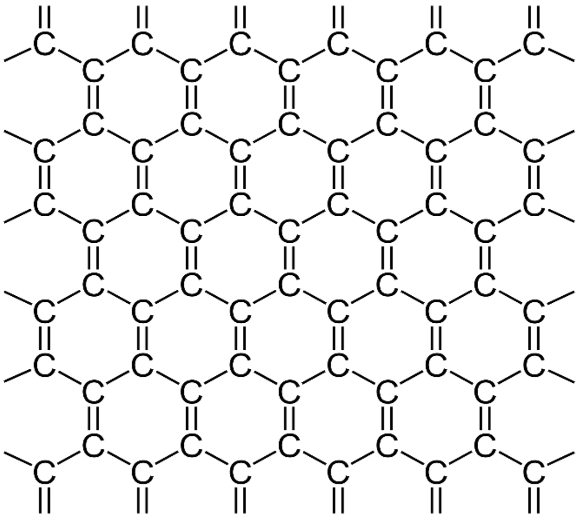

Figure 11: Structure of graphene.

Figure 12. It can be wrapped up into 0D fullerenes, rolled into 1D nanotubes, or stacked into 3D graphite [17].

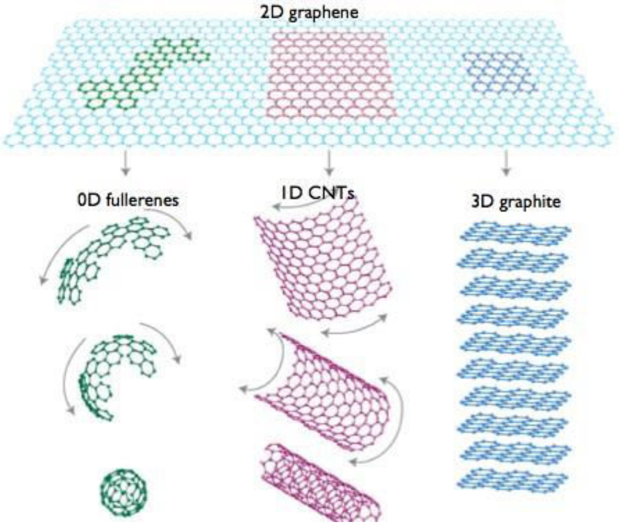

Figure 12: Graphene as building block for 0, 1 and 3D materials [17].

Due to exceptional properties stated above graphene has great potential for improving mechanical, electrical, thermal, and gas barrier properties of polymers.

CHAPTER 2

LITERATURE REVIEW

2.1 Crystallization kinetics models

A number of theoretical models have been proposed for studying isothermal and nonisothermal crystallization of polymers and their composites. The kinetics of crystallization of polymers is generally studied using techniques like differential scanning calorimetry (DSC) and thermogravimetric analysis (TGA). These equipments are run either on isothermal or nonisothermal mode. The main purpose is to evaluate kinetic parameters such as activation energy and rate constants etc. In principle the methods to analyze these data can be broadly classified as isokinetic methods and isoconversional methods. In isokinetics methods the kinetic parameters are supposed to be constant throughout the whole experiment and same transformation mechanism is applicable on whole set of data while in isoconversional methods the transformation rate is a function of temperature at constant conversion. Some of the models are as follows,

2.1.1 Avrami model

Avrami proposed a model to describe isothermal kinetics of polymers. The change in crystallinity with time is given by:

$$X_t = 1 - \exp(-k(T)\, t^n) \qquad (1)$$

Here X_t is relative crystallinity, k is rate constant, n is Avrami index and T is crystallization temperature. To plot the relative crystallinity profile, Equation 1 can be converted to logarithmic form as follows:

$$\ln(-ln\,(1 - X_t)) = n \ln T + \ln k \tag{2}$$

Plot of *ln* (-*ln* (1-X_t)) versus *ln* T gives straight line with intercept k and slope n.

2.1.2 Jeziorny model

Jeziorny proposed the following equation;

$$\frac{dX_t}{dt} = k'(T) \times (1 - X_t) \tag{3}$$

where

$$lnk'(T) = \frac{lnk}{\beta} \tag{4}$$

Here k is Avrami-Erofeev isothermal crystallization rate constant, $k'(T)$ is corresponding nonisothermal analogue and β is heating rate. X_t is temperature dependent relative crystallinity and t is crystallization time. Plot of *ln*(-*ln*(1-X_t)) versus ln*t* gives n.

2.1.3 Ozawa model

For nonisothermal crystallization of polymers Ozawa proposed a model. The degree of crystallinity is given by as a function of temperature:

$$X_t = 1 - \frac{e^{-k(T)}}{\beta^m} \tag{5}$$

Here m is Ozawa exponent, β is cooling rate and *k(T)* is cooling function. The above equation is linearized using double logarithm and is given by:

$$\ln(-\ln(1-X_t)) = \ln\big(k(T)\big) - m\, ln(\beta) \tag{6}$$

According to above equation if Ozawa model describes correctly the crystallization behaviour of the polymer, plot of $\ln(-\ln(1-X_t))$ with respect to $ln(\beta)$ should give straight line with slope m and intercept $\ln\big(k(T)\big)$.

2.1.4 Mo model

Liu et al. proposed a model to describe the nonisothermal behaviour of polymers. This model is actually combination of Avrami and Ozawa models. The Avrami equation is given by:

$$X_t = 1 - e^{-k(T)t^n} \tag{7}$$

Linearizing this equation gives:

$$\ln(-\ln(1-X_t)) = n\ln(t) + \ln(k_t) \tag{8}$$

Combining Equations 6 and 8 gives model proposed by Liu et al.:

$$n\ln(t) + \ln(k_t) = \ln\big(k(T)\big) - m\ln(\beta) \tag{9}$$

Further simplification of above equation gives:

$$\ln(\beta) = \ln\big(F(T)\big) - \alpha\ln(t) \tag{10}$$

The above described models have been extensively use to study crystallization kinetics of polymers and their composites. However they have certain limitations and drawbacks. They are not mechanistic; they are empirical; and they lack fundamental and phenomenological formalism. The model parameters do not always have adequate physical significance. Some of them do not represent the entire crystallization profile, and some experience double logarithm insensitivity and linearization problems.

2.1.5 Nonisothermal Avrami-Erofeev mechanistic model

Avrami-Erofeev model overcomes all drawbacks of traditional models and has been used in this study. This is based on mechanistic consideration. It applies to the entire DSC nonisothermal crystallization curve. The model-predicted kinetic parameters—apparent kinetic energy E_a, Avrami exponent n, and crystallization frequency factor k_0—have physical significance.

2.1.5.1. Avrami-Erofeev model

A new nonisothermal crystallization model [21] for crystalline polymer using the Avrami-Erofeev equation was published by us in 2013. This model, with detailed assumptions and mathematical derivation, is reported in the above reference. Here, a summary is provided as follows.

The nonisothermal Avrami-Erofeev polymer crystallization rate, involving nucleation and growth, can be written as:

$$\frac{d\alpha}{dT} = \frac{k_0}{\beta} \times \exp\left[-\frac{E_a}{R}\left(\frac{1}{T} - \frac{1}{T_0}\right)\right] \times n(1-\alpha)\left[-\ln(1-\alpha)\right]^{\frac{n-1}{n}} \tag{11}$$

where we define the following:

$$f(\alpha) = n(1-\alpha)\left[-\ln(1-\alpha)\right]^{\frac{n-1}{n}} \tag{12}$$

$$k'(T) = k_0 \times \exp\left[-\frac{E_a}{R}\left(\frac{1}{T} - \frac{1}{T_0}\right)\right] \tag{13}$$

$$E_a(apparentcrystallizationenergy) = E_{grow} - E_{nucl} \tag{14}$$

$$k_0(overallcrystallization\ frequencyfactor) = \left(\frac{k_s N_0}{V_0}\right)\frac{k_{grow,0}}{k_{nucl,0}} \neq f(T) \tag{15}$$

$$k_{grow}(T) = k_{grow,0} \times \exp\left[-\frac{E_{grow}}{R}\left(\frac{1}{T} - \frac{1}{T_0}\right)\right] \tag{16}$$

$$k_{nucl}(T) = k_{nucl,0} \times \exp\left[-\frac{E_{nucl}}{R}\left(\frac{1}{T} - \frac{1}{T_0}\right)\right] \tag{17}$$

In the above equations, $f(\alpha)$ is called Avrami-Erofeev nonisothermal crystallization function, and α is the temperature- or time-dependent volume fraction of the molten polymer solidified due to cooling. Therefore, α concerns the phase morphology of the whole sample (melt plus solid). It is called relative crystallinity or degree of crystallization. β is the cooling rate. n is the dimension of the growing crystal. N_o is the number of germ nuclei, that is, the potential nucleus formation sites/defects. V_o is the initial volume of the molten polymer. K_s is the shape factor for the growing nuclei. $k_{grow,0}$ and E_{grow} are the frequency factors and activation energy of crystal growth, respectively. $K_{nucl,0}$ and E_{nucl} represent the corresponding terms for nucleation, respectively. R is the universal gas constant, and T_o is the centering temperature.

The Avrami index n, in Equation 18, illustrates two aspects—the crystal dimension and the nature of nucleation process. Therefore, n is written in terms of the following two components [22]:

$$n = n_d + n_n \tag{18}$$

where n_d shows the dimension of the growing crystals. Theoretically speaking, n_d can be only integers—1, 2, and 3—that correspond to one-,two-,and three-dimensional crystals formed, respectively; and n_n represents the nucleation process. In principle, it should be 0 or 1, where 0 refers to instantaneous (athermal/heterogeneous) nucleation; and 1, to sporadic (thermal/homogeneous) one. For many systems, the model-predicted n turns out to be a non-integer which is attributed to $0 \leq n_n \leq 1$. This means the simultaneous occurrence of instantaneous and sporadic nucleation processes [23]. A balance between thermodynamic and kinetic factors influences the value of n_n [24].

$\alpha(T)$ is related to the corresponding weight fraction relative crystallinity $\alpha_w(T)$ through the following expression [21]:

$$\alpha = \frac{\alpha_w}{\alpha_w + {}^{\rho_c}\!/_{\rho_a}\left(1-\alpha_w\right)} \tag{19}$$

where ρ_c and ρ_a are the densities of the crystalline and amorphous phases, respectively. For polypropylene, the values of ρ_c and ρ_a have been reported earlier. The relation α versus T is called relative crystallinity or degree of crystallization profile.

α_w can be calculated from a typical constant cooling rate nonisothermal DSC experiment by using Equation 20:

$$\alpha_w = \frac{\Delta H(T)}{\Delta H_{total}} = \frac{\int_{T_i}^{T}\left(\frac{dH}{dT}\right)dT}{\int_{T_i}^{T_\infty}\left(\frac{dH}{dT}\right)dT} \tag{20}$$

where ΔH_{total} is the maximum enthalpy value reached at the end of the nonisothermal crystallization process and $\Delta H(T)$ is the enthalpy evolved as a function of crystallization temperature T. T_i and T_∞ represent the crystallization start and completion temperatures, respectively. ΔH_{total} and $\Delta H(T)$ both can be acquired through the software of a standard differential scanning calorimeter (DSC). Using Equation 19, the DSC-generated α_w can be converted to the corresponding volume fraction α.

The experimental confirmation of the above new non-isothermal crystallization model is available in one of our recent publications [25]. See Harkin-Jones et al. [26] that comprehensively reviews the literature models.

2.1.5.2. Solution of Avrami-Erofeev model

We solved Equation 11 numerically, and estimated the kinetic triplet (k_o, n, and E_a) as follows. First, we modified it through separation of variables, and integrated the left hand side (LHS) analytically, and transformed the right hand side (RHS) into the well-known *temperature integral* $\int \exp\left(-\frac{E_a}{RT}\right)dT$. See Equations 21 and 22. Next, we converted the temperature integral into a real part and an exponential integral part. See Equation 23. This is how we integrated the temperature integral, which we finally transformed to the non-linear algebraic form. We solved this modified model equation using the *Mathematica 8.0 Nonlinear Model Fit* software. $T_o = 370$ K was used as the centering temperature. The LHS of Equation 23, containing $-\ln(1-\alpha)$, has a point of discontinuity at $\alpha_{final} = 1$. This was resolved by approximating $\alpha_{final} \cong 0.9999$. Depending on the cooling rates, 30 to 45 experimental data points were considered for kinetic parameter estimation.

$$\int \frac{d\alpha}{n(1-\alpha)[-\ln(1-\alpha)]^{\frac{n-1}{n}}} = \int \frac{k_0}{\beta} \times \exp\left[-\frac{E_a}{R}\left(\frac{1}{T}-\frac{1}{T_0}\right)\right] dT \tag{21}$$

$$[-\ln(1-\alpha)]^{\frac{1}{n}} = \frac{k_0 \exp\left(\frac{E_a}{RT_0}\right)}{\beta} \int \exp\left(-\frac{E_a}{RT}\right) dT \tag{22}$$

$$[-\ln(1-\alpha)]^{\frac{1}{n}} = \frac{k_0 \exp\left(\frac{E_a}{RT_0}\right)}{\beta} \left[T \exp\left(-\frac{E_a}{RT}\right) + \frac{E_a\, Ei\left(-\frac{E_a}{RT}\right)}{R} \right] \tag{23}$$

where $Ei\left(-\frac{E_a}{RT}\right)$ is the exponential integral of $-\frac{E_a}{RT}$.

We estimated the model parameters considering the following statistical criteria—95% confidence interval, coefficient of determination (R^2), estimated variance, and standard error. The aforementioned *Mathematica* software eventually generates them. Convergence was accepted when the objective function changed less than the specified tolerance of 10^{-8}. For the sake of brevity and sufficiency, we list only R^2 for each of the estimated kinetic parameters.

2.2 Crystallization models applied to semicrystalline polymers

The process of crystallization occurs in polymers when they are cooled from melt and is associated with the partial alignment of molecular chains of polymers. When a polymer especially semicrystalline polymer is solidified from melt, due to long molecular length of polymeric chains and their difficulty of parallel alignment, it is difficult to form an ordered crystal structure. This is actually origin of semicrystalline polymers. Different models proposed for semicrystalline polymers are as follows,

2.2.1 Fringed micelle model

This is one of the earliest models for semicrystalline polymers which is based on two phase systems of amorphous and crystalline regions. Amorphous regions are made up of disordered conformations while crystalline region comprised of stacks of parallel aligned chains Figure 13 [27,28].

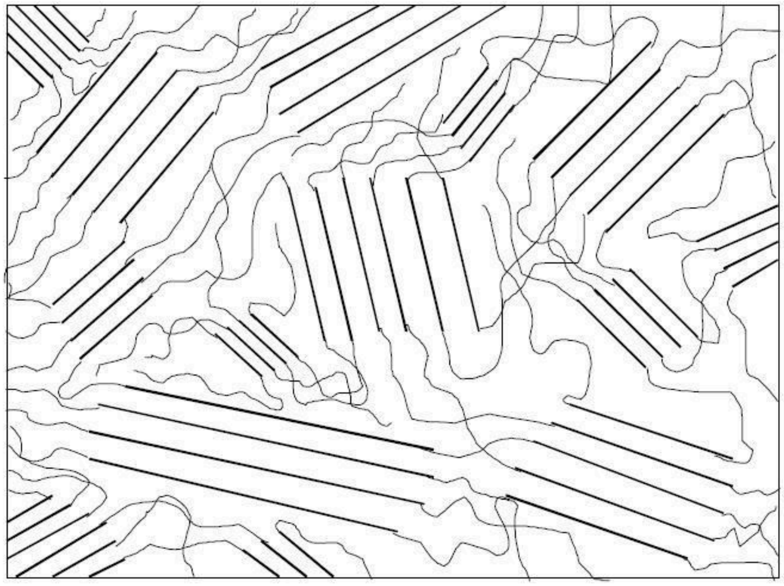

Figure 13: Fringed Micelle model for polymers [27].

2.2.2 Chain folding model

It was reported by Keller that the polyethylene single crystals grown from dilute solution observed under an electron microscope appear in the form of lamella or thin plates Figure 14. Diffraction studies on these thin plates revealed that the chain axes are directed more or less perpendicular to the basal faces. Given the extended length of a polymer chain, it was proposed that a chain must traverse a given crystallite many times to conform to both of the above observations. This led to the concept of chain folding in semicrystalline polymers [29,30].

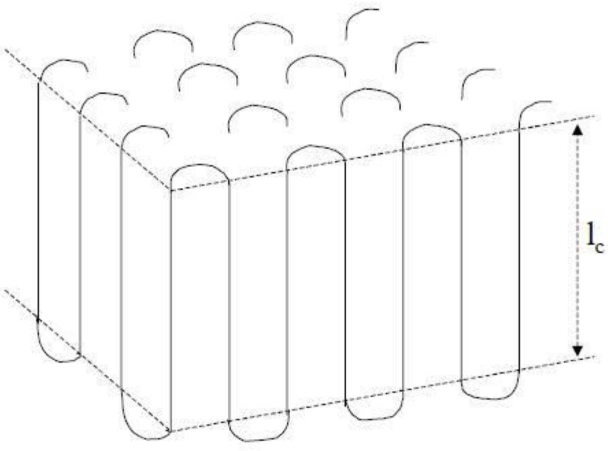

Figure 14: Regularly folded lamellar structure [30].

2.3 Flory's thermodynamic theory of crystallization applied to *i*-PP

The Flory's thermodynamic theory considers copolymers having A and B units in which B is not able to enter in the imaginary lattice. The comonomer units are assumed to be defects and should not be considered in the growing crystal. Polymer melt consists of both A and B units and crystalline part is completely formed by A units. It is observed that at a given temperature there always exists a limiting sequence length n^* of crystalline part which is in equilibrium with melt [21,22].

Now, we first summarize the microstructural defects of a typical Ziegler-Natta (Z-N) *i*-PP. Ti-based Z-N catalysts, in the presence of internal and external donors, synthesize *i*-PP predominantly with stereo-defects introduced in the crystallizable isotactic propylene sequence of the backbone [33–35]. The origin of stereo-defects has been elaborated elsewhere in the literature [36]. This makes the *i*-PP backbone resembling that of, for example, a typical ethylene–α-olefin copolymer where the α-olefin introduces branching defects in the ethylene sequence of the backbone. Hence, an *i*-PP can be microstructurally defined to be a random stereo-copolymer with configurational defects along the backbone [34,36,37]. See Scheme 1. Accordingly, the *i*-PP stereo-defect disrupts the backbone as the addition of the α-olefin does in polyethylene [36]. Therefore, Flory's copolymer equilibrium theory [31,38,39] can also be applied to the stereo-irregular Z-N *i*-PP [34].

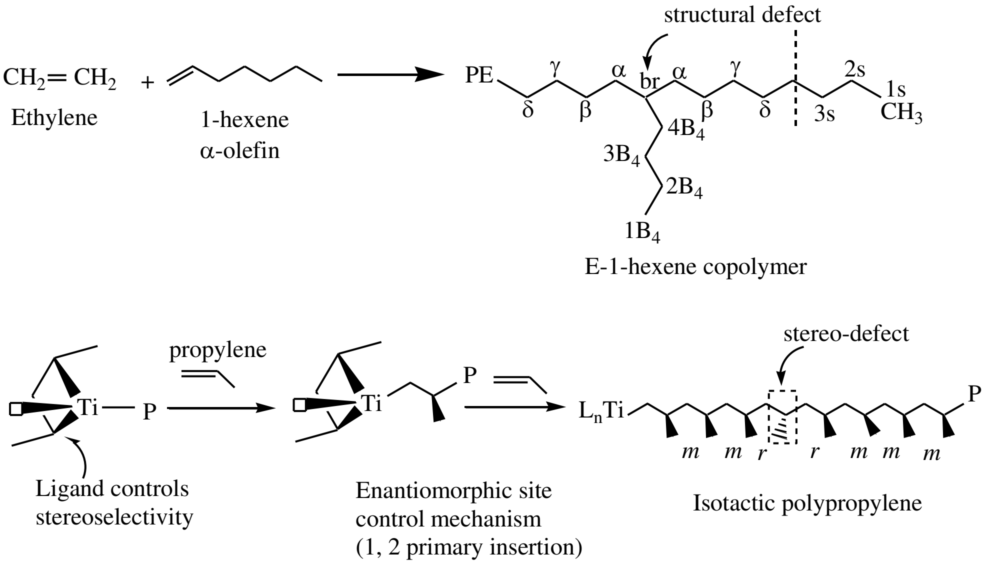

Scheme 1. Comparison of the stereo-defect of an *i*-PP with the structural defect of a typical ethylene–α-olefin copolymer. The *i*-PP stereo-defects originate from enantiofacial error, chain-end epimerization, and chain-end effect [34].

In a random ethylene–α-olefin copolymer, the ethylene perpetuation probability p, that is, the probability that a crystallizable unit is succeeded by another such unit is given by $[X_E + (1 - X_E)/2]$ where X_E is the average ethylene mole fraction [40,41]. The term $(1-X_E)/2$ is the correction due to the incorporation of one $-CH_2-$ unit (or half C_2H_4 unit) per insertion of one α-olefin comonomer and exclusion of the pendant alkyl group (greater than methyl) from the chain fold. As per Scheme 1 and what is stated above, for an *i*-PP, the analogous propylene perpetuation probability p can be approximated by the crystallizable isotacticity index X_{mmmm} (meso-pentad) mole fraction.

According to the above description and Flory's copolymer equilibrium theory, the propylene perpetuation probability p can be related to the critical (limiting) sequence number $n^*(T)$ of the stable crystallite, that equilibrates with the melt at a given temperature, using the following equations [31,38,39]:

$$n^*(T) = \frac{-1}{\theta + \ln p}\left[\ln\left(\frac{DX_{mmmm}}{p}\right) + 2\ln\left(\frac{1-p}{1-e^{-\theta}}\right)\right] \tag{24}$$

where

$$\theta\,(level\,of\ undercooling) = \frac{\Delta H_u}{RT_m^0}\frac{T_m^0 - T}{T} = \frac{\Delta H_u}{RT_m^0}\frac{\Delta T}{T} \tag{25}$$

$$D\,(crystal\,surface\,free\,energy\,effect) = e^{-2\sigma_e a_o / RT} \tag{26}$$

where X_{mmmm} is the mole fraction of the crystallizable (meso-pentad) isotacticity index; R is the universal gas constant; and T is cooling temperature in K. θ is measure of undercooling and D is crystal surface free energy and p is sequence propagation probability of A units.

Note that n^*, θ, and D are dimensionless. Therefore, they offer a common footing to compare the melt behavior and crystallization of *i*-PPs of different structures under varying experimental conditions. In Equation 25, T_m^0 (459.1 K) is the melting point of an isotactic polypropylene perfect crystal (completely defect-free *i*-PP of infinite lamellar thickness and molar mass). This is also called polypropylene equilibrium melting point. ΔH_u (2100 cal/mol = 2×10^9 erg/cm^3) is the heat of fusion for perfect crystal *i*-PP repeat unit $-[CH_2-CH(CH_3)]-$, σ_e (96 erg/cm^3) is the polypropylene basal/fold free surface energy, and a_o (2.05×10^5 m^2/mol) is the cross-sectional area of a polypropylene chain [38,42,43]. All these properties relate to *alpha*-phase *i*-PP. For a constant cooling rate nonisothermal DSC crystallization process, $n^*(T)$ evaluates the temperature-dependent dynamic critical crystallite stability. Only isotactic propylene sequences, greater than $n^*(T)$, form stable crystals. With increasing temperature, the crystals melt and $n^*(T)$ increases, and $n^* \to \infty$ represents the thickest possible crystals [39].

For the random stereo-irregular Z-N *i*-PP—a random stereo-copolymer with configurational defects—Flory's weight fraction equilibrium crystallinity f_c is given by [31,39]:

$$f_c = \frac{X_{mmmm}(1-p)^2 p^{n^*-1}\left[\frac{p}{(1-p)^2} - \frac{e^{-\theta}}{(1-e^{-\theta})^2} + n^*\left[\frac{1}{1-p} - \frac{1}{1-e^{-\theta}}\right]\right]}{1 - X_{mmmm} p^{n^*-1}\left[\frac{1-p}{1-e^{-\theta}}\right]^2 \left[n^*(1-e^{-\theta}) + e^{-\theta}\right]} \quad (27)$$

Equation 27 is the revised version of the original derivation by Flory [31]. For a defect-free *i*-PP, $p = X_{mmmm}$ (mole fraction) = 1, which as well gives $f_c = 1$ under this situation.

2.4 Melting and crystal lamellar thickness distribution

The lamellar thickness *L* of folded chain crystal (FCC) of the experimental Z-N *i*-PP-a random stereo-copolymer [44–46] with configurational defects along the backbone-was calculated using the following version of Gibbs-Thompson thermodynamic equation [41,47–50]:

$$L = \frac{2\sigma_e}{\Delta H_u}\left(\frac{T^0_{m,i-PP}}{T^0_{m,i-PP} - T_m}\right) \tag{28}$$

where $T^0_{m,\,i-PP}$ is the equilibrium melting temperature of an *i*-PP with stereo-defects, and T_m is the DSC-measured Cycle 3 melting temperature. ΔH_u and σ_e have been already defined in Equations 25 and 26, respectively. Equation 28 corrects for the stereo-defects in the *i*-PP backbone. Here, the *i*-PP pendant -CH3- group, with that in the stereo-defect, is included in the folded lamella [39,46,51]. Under such a situation, Cheng et al. [46], using thermodynamic considerations, derived the following equation:

$$T^0_{m,\,i-PP} = T^0_m\left[1 - \frac{(1 - X_{mmmm})\varepsilon_0}{\Delta H^0_f}\right] \tag{29}$$

where ε_0 (1.90 kJ/mol) is the excess energy of a perfect *i*-PP crystal. X_{mmmm}, T^0_m , and ΔH^0_f have been already defined in Equations 24, 25, and 26, respectively. The standard deviation (STD), calculated by using Equation 30, is 1.33.

$$STD = \sqrt{\frac{1}{N_{data}}\sum_{1}^{N_{data}}\left[T^0_{m,i-PP}(Experimental) - T^0_{m,i-PP}(Equation20)\right]^2} \tag{30}$$

The following alpha-phase perfect crystal (of infinite lamellar thickness and molar mass) parametric values [38,42,43] were applied to the above equations: T_m^o = 459.1 K, ΔH_f^o = 8786.4 J/mol (207 J/g), and σ_e (crystal specific surface free energy) = 0.096 J/m^2.

L was estimated using Equations 28 and 29, and the corresponding mass fraction m_{T_j} (at a given temperature T_j), by applying Equation 31 and the Cycle 3 DSC data [25]:

$$m_{T_j} = \frac{\int_{T_i}^{T_j} \left(\frac{dH}{dT}\right) dT - \int_{T_i}^{T_{j-1}} \left(\frac{dH}{dT}\right) dT}{\int_{T_i}^{T_\infty} \left(\frac{dH}{dT}\right) dT} \qquad (31)$$

CHAPTER 3

MATERIALS AND METHODS

3.1 Materials

The pristine isotactic polypropylene (PP H1030) used in this study was supplied by National Industrialization Company (Tasnee), Saudi Arabia. As per the Tasnee data sheet, it has a melt flow rate (MFR) of 3 g/10 min at 230 ºC and 2.16 kg load. The melting temperature and density are 163 ºC and 0.900 g/cm^3, respectively. Graphene Nanoplatelets (GNPs) having trade name of GRAFEN®-GNP was supplied by Grafen Chemical Industries Co., Turkey. GNPs have average thickness 5–15 nm, average particle diameter 10-20 µm, oxygen content < 5% and 95% purity. GNPs were used as received, without any modifications. The antioxidant Irganox 1010 supplied from BASF was also added into the composite as a heat stabilizer.

3.1.1 Fabrication of *i*-PP/graphene nanocomposites

Nanocomposites of *i*-PP with different GNP contents (0.1, 0.5, 1.0, 1.5, 2.0, 2.5 and 3.0 wt %) and Irganox 1010 (0.1 wt %) were fabricated using melt-blending technique using a minilab twin-screw extruder (HAAKE Minilab II) Figure 15. After dry blending the components were mixed in extruder at 190 ºC with screw speed of 100 rpm for 10 minutes. As reference, pristine *i*-PP samples were also similarly processed for property studies.

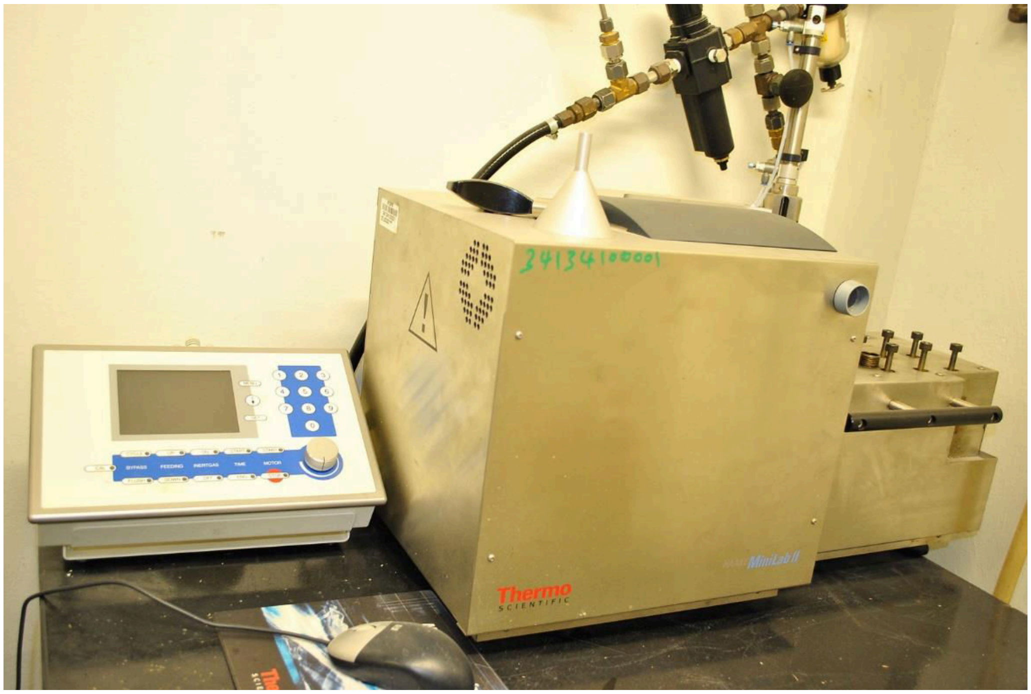

Figure 15: Minilab twin screw extruder.

3.1.2 Characterization of *i*-PP and *i*-PP/graphene nanocomposites

4.2.2.1. Differential scanning calorimetry

The thermal properties of the experimental *i*-PP and *i*-PP/GNP nanocomposites were measured in terms of peak melting (T_{pm}) and crystallization (T_{pc}) temperatures, and % crystallinity (X_c) using a differential scanning calorimeter (DSC Q2000, Texas Instrument) Figure 16. The instrument was calibrated using indium. The three-cycle (heating-cooling-heating) experimental procedure reported in the literature was followed [52–54]. About 5.50 mg *i*-PP (and *i*-PP/GNP composites sample) flake sample was taken in an aluminum pan and was tightly crimped with a lid. A similar empty pan was used as a reference. The following heating/cooling rates-5.0, 10.0, 12.5, 15.0, and 20.0 ^{o}C/min-were used under nitrogen flow. After keeping the sample and reference pans in the DSC instrument, Cycle

1 was completed as follows to remove thermal history and recrystallization. The sample was first heated from room temperature to 200.0 ºC at a selected heating rate; then it was kept at this temperature for 5 min. In Cycle 2, it was cooled to room temperature at the same ramp. Finally, in Cycle 3, the sample was heated to 200.0 ºC, also using the same heating rate. This means that Cycles 1 to 3 experienced the same heating or cooling rate in a typical DSC run.

Figure 16: Differential Scanning Calorimetry.

The data were acquired for each cycle and handled using the TA explorer software. The %crystallinity was determined using Cycle 3 DSC output and the following relation: $\chi_c = (\Delta H_f/\Delta H_f^{\circ}) \times 100$, where ΔH_f and ΔH_f° (207 J/g) [38,42,43] are the heats of fusion of the experimental sample and the perfect (defect-free) *i*-PP crystal (of infinite lamellar thickness and molar mass), respectively. The measured χ_c was subsequently used to calculate the material density ρ_{polym}, following the rule of additivity of volumes of polypropylene amorphous and crystalline phases [55]: $\chi_c = (1/\rho_{polym} - 1/\rho_a)/(1/\rho_c - 1/\rho_a)$; where ρ = density; *a* = amorphous phase; *c* = crystalline phase; and *polym* = polymer. For polypropylene, ρ_c = 0.950 g/mL and ρ_a = 0.850 g/mL [42]. Next, the amorphous volume fraction ϕ_a was estimated using the relation $\phi_a = (\rho_c - \rho)/(\rho_c - \rho_a)$.

4.2.2.2. Gel permeation chromatography

The experimental *i*-PP was characterized in terms of weight average molecular weight (MW) and polydispersity index (PDI), using a Viscotek multidetector high temperature Gel Permeation Chromatography (HT GPC Module 350A) instrument Figure 17. The column temperature was set at 140 °C. The polypropylene sample (about 21.50 mg), taken in a 40 mL glass vial, was dissolved in 10.0 mL butylated hydroxy toluene BHT-stabilized-1,2,4 trichlorobenzene (TCB) as follows. The vial was closed with a Teflon cap. Then the sample was completely dissolved by placing it into the Vortex Auto Sampler for 3 hr at 140 ^{0}C under mild stirring.

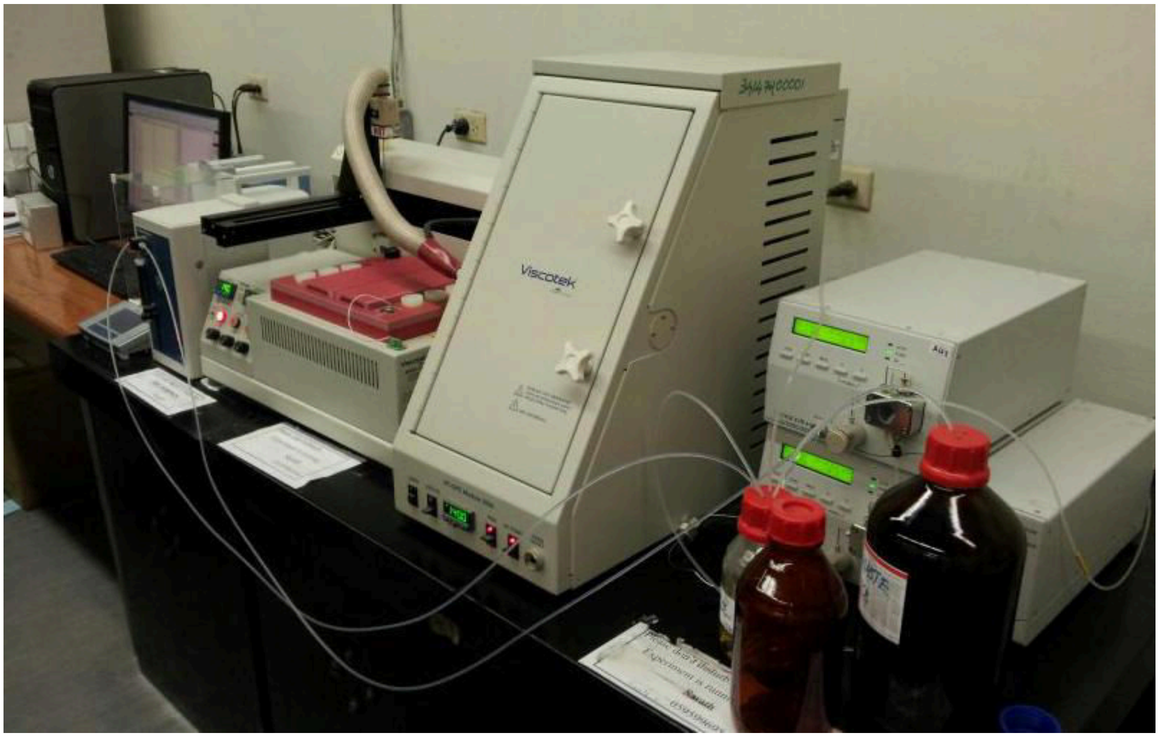

Figure 17: Gel Permeation Chromatography.

Before injecting a sample, all the detectors—refractive index (RI) detector, and low angle and right angle light scattering (LALS and RALS) detectors—and the inlet pressure (IP), and the differential pressure (DP) cells were purged for 3 hr using TCB to obtain a stable baseline. The flow rate of TCB was 1.0 mL/min. The experimental *i*-PP sample, having a concentration of 2.15 mg/mL, was injected into the system. The run time was 60 min. Viscotek OmniSEC software acquired the response data, generated by the LALS and RALS detectors, and calculated the weight average molecular weight M_w and the PDI.

4.2.2.3. Carbon-13 nuclear magnetic resonance

The microstructural parameters (meso-pentad mole fractions) of the experimental *i*-PP were determined using Carbon-13 Nuclear Magnetic Resonance (^{13}C NMR) spectroscopy. For this, a Bruker 600 MHz spectrometer was used. The sample was prepared at 120 °C by dissolving about 250 mg of the sample in a 10 mm NMR tube using 3 mL of the deuterated dimethyl sulfoxide (DMSO-d_6)/trichlorobenzene (TCB) 10/90 % (v/v) mixed solvent. The DMSO-d_6 was used as an internal lock.

The spectrum was recorded at 120 ºC using WALTZ-16 decoupler, 30º pulse angle with pulse repetition time of 10 s. The free induction decays (FIDs) were stored in 32 K data points using a spectral width of 70 ppm. The experimental data were processed and analyzed using TOPSPIN software (version 2.0).

The spectral region of methyl carbon signals (22.60–19.50 ppm) was divided into three triad configurational sequences, that is, *mm* (22.60–21.10 ppm), *mr* (21.10–21.40 ppm), and *rr* (21.40–19.50 ppm). Each of the above triad regions was further split into three pentad configurational sequences using Lorentzian distribution functions [56].

4.2.2.4.Crystallization analysis fractionation

Crystallization Analysis fractionation (CRYSTAF) was performed in a model 200 instrument from Polymer Char S.A (Figure 18). Standard conditions were used in all the analyses with a starting solution concentration of 0.1% (w/w), 30 mg in 30 ml of 1,2,4 trichlorobenzene (TCB), and a crystallization rate of 0.1 °C/min [57].

Figure 18: CRYSTAF.

CHAPTER 4

Nonisothermal crystallization and melt behavior of *i*-PP

4.1 Nonisothermal crystallization using Avrami-Erofeev model

A review of the literature on overall polypropylene thermal behavior shows the following. The published nonisothermal crystallization studies relate to *i*-PP with and without nucleating agents [58–61] and *i*-PP/inorganic filler micro- and nanocomposites [62–65]. Here, the crystallization kinetics was investigated using Caze-Chuah, Jeziorny, Ozawa, Mo, and Seo-Kim models (as appropriate) [58–65]. However, the following can be commented regarding these models. They are not mechanistic; they are empirical; and they lack fundamental and phenomenological formalism. The model parameters do not always have adequate physical significance. Some of them do not represent the entire crystallization profile, and some experience double logarithm insensitivity and linearization problems. See Reference [21] for the details.

We particularly summarize the study by Alamo et al. [38] who investigated, among several subjects, the effects of chain-walking defects on *i*-PP %crystallinity and melting point, considering Flory's equilibrium theory. These regio-defects, resulting from 3, 1 enchainment, were introduced into the polymer backbone by polymerizing propylene using selected nickel α-diimine precatalysts and methylaluminoxane (MAO) cocatalyst. They lowered the above thermal properties with reference to the corresponding Flory's equilibrium values. However, these authors did not investigate the influence of *i*-PP regio-defects on nonisothermal crystallization kinetics, which is an important subject.

We observe that the aforementioned *i*-PP nonisothermal crystallization studies and the report by Alamo et al. [38] did not study the *i*-PP dynamic melting behavior and crystallization from Flory's equilibrium theory perspective, particularly considering the following three temperature-dependent dimensionless factors—level of undercooling θ, crystal surface free energy D, and critical stable crystallite sequence number n^*. Our focused objective is the following. Can the integration of the fundamental mechanistic crystallization model (which we published in 2013) [21], Flory's thermodynamic equilibrium theory [31,38,39], Gibbs-Thompson equation [41,47–50], and DSC experiments generate new and/or better insightful results, interpretations, and explanations regarding nonisothermal *i*-PP crystallization and melt process? Note that such an integrated conceptual framework to study the overall polyolefin thermal behavior, as far as we know, has not been yet published. Therefore, we undertake this study. The merits of our above crystallization model over the other literature models are well documented [21]. This is based on mechanistic consideration. It applies to the entire DSC nonisothermal crystallization curve. The model-predicted kinetic parameters—apparent kinetic energy E_a, Avrami exponent n, and crystallization frequency factor k_0—have physical significance.

We plan to pursue the above objective by correlating the relative crystallinity α, temperature-dependent instantaneous crystallinity χ, E_a, crystal dimension n_d, nucleation mode n_c, k_0, and the lamellar thickness and melting temperature, as appropriate, to θ, D, and n^*. The DSC experiments, as a function of heating/cooling rates, will be conducted using an *alpha*-phase commercial Ziegler-Natta *i*-PP without adding a nucleating agent.

The results obtained from DSC, GPC, results of lamellar thickness distribution parameters and Tasnee datasheet properties of *i*-PP are summarized in Table 3 below.

Table 3: Summary of the experimental *i*-PP properties.

	Heating/cooling rates β (°C/min)				
Properties	**5.0**	**10.0**	**12.5**	**15.0**	**20.0**
Weight average molecular weight M_w[a] (g/mol)	427,500				
Polydispersity index (PDI)[a]	4.9				
Viscosity average molecular weight M_v[b] (g/mol)	440,500				
Peak melting point T_{pm} (°C)	161.7	160.7	161.1	161.7	160.7
Peak crystallization point T_{pc} (°C)	119.9	113.0	116.3	115.8	114.5
Crystallinity χ_c (%) 3rd cycle	44.54	46.57	46.34	46.70	44.68
Crystallinity χ_c (%) 2nd cycle	59.07	56.23	55.91	59.27	55.31
i-PP material density ρ_{poly} (g/cm^3)	0.893	0.899	0.895	0.904	0.895
Amorphous volume fraction ϕ_a	0.579	0.517	0.562	0.464	0.555
Weight average lamellar thickness $L_{WAV\ DSC\ GT}$ (nm)	7.1	6.9	6.4	6.7	6.1
Most probable lamellar thickness $L_{MP\ DSC\ GT}$ (nm)	6.7	6.8	6.8	6.8	6.7
Variance of LTD σ_{LTD} (nm)	2.8	2.8	2.5	2.7	2.5
Most probable T_{MP} (K)	446.0	442.5	440.0	438.5	437.0
Level of undercooling θ_{MP}	0.37	0.35	0.33	0.31	0.28
Crystal surface free energy $D_{MP} \times 10^6$	26.8	25.3	24.5	24.0	22.0
Tasnee data sheet properties					
Melt flow rate MFR (g/10 min)	3.00				
i-PP material density ρ_{poly} (g/cm^3)	0.900[c]				

[a] Measured using GPC with light scattering detector.

[b] Estimated from the work of Grein et al.[66] Comparable with measured GPC M_w.

[c] Matches very well the values determined by DSC.

ρ_{poly} is comparable with that of Tasnee data sheet.

Properties such as T_{pm}, T_{pc}, χ_c, ϕ_a, $L_{WAV\ DSC\ GT}$, $L_{MP\ DSC\ GT}$, T_{MP}, θ_{MP}, and D_{MP} are fairly invariant of cooling/heating rates.

Now we evaluate the present nonisothermal Avrami-Erofeev model performance, and discuss the significance of the major pertinent results. Figure 19 compares the model

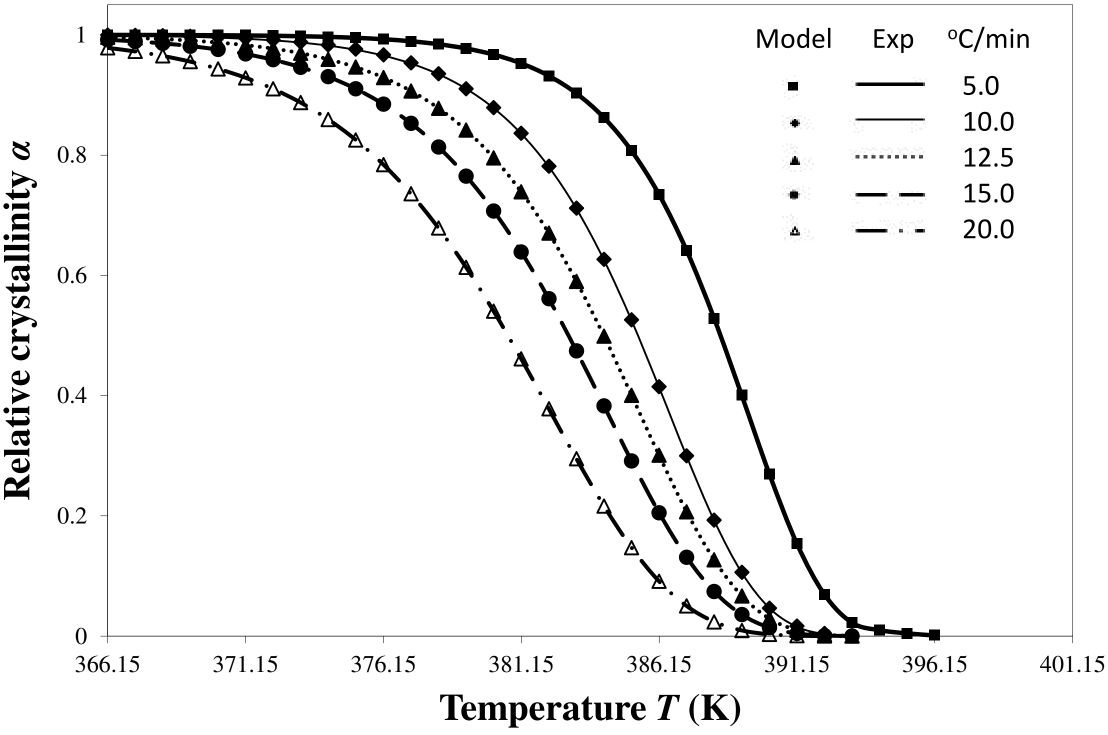

Figure 19: Comparison of model-predicted *i*-PP relative crystallinity profiles with DSC experiments for different cooling rates.

predicted relative crystallization profiles, determined using Equation 11, with the corresponding DSC profiles at different cooling rates. The agreement between model and experiment, in each case, is excellent. The crystallization profiles shifted leftward with the increase in cooling rate β. This trend matches that of the cooling rate-dependent nonisothermal *i*-PP relative crystallinity profiles reported in the literature [26,67]. Our premier model finding is the following. A single value of n represents the whole crystallization regime (primary as well as secondary). This result signifies that the same mechanism of nucleation and crystal growth holds, irrespective of the cooling rates, all throughout the nonisothermal *i*-PP crystallization. This argues how the present model overcomes the drawbacks and limitations of the arbitrary parameter-based existing nonisothermal crystallization models, summarized in our previous study [21]. Also, see Harkin-Jones et al. [26] that reviews the parametric nonisothermal crystallization literature models. Therefore, the assumption of change in crystallization mechanism, as reported in the literature [26,68–71], is invalid.

Table 4: Model predicted crystallization kinetics parameters.

DSC cooling rates °C/min	**Crystallization kinetics parameters**	***i*-PP homopolymer**
5.0	n k_o (min^{-1}) E_a (kJ/mol) R^2	3.50 0.20 123.06 0.9904
10.0	n k_o (min^{-1}) E_a (kJ/mol) R^2	3.00 0.54 123.63 0.9891
12.5	n k_o (min^{-1}) E_a (kJ/mol) R^2	2.60 0.75 123.55 0.9858
15.0	n k_o (min^{-1}) E_a (kJ/mol) R^2	2.38 1.02 123.71 0.9886
20.0	n k_o (min^{-1}) E_a (kJ/mol) R^2	2.13 1.69 123.56 0.9881

Table 4 shows that the model-predicted n_d ranges between 2 and 3, and it depends on the cooling rates. For β = 5.0 and 10.0 °C/min, n_d = 3; and for β = 12.5, 15.0, and 20.0 °C/min, n_d = 2. Hence, the resulting *i*-PP crystal dimension varies between spherical and cylindrical, that is, two and three dimensional alignments of the polymer backbone lamellae, corresponding to low and high cooling rates, respectively. Further, n has an integral part n_d and a fractional part n_n. Therefore, according to Equation 18, for the subject *i*-PP, instantaneous (athermal/heterogeneous) as well as sporadic (thermal/homogeneous) nucleations ($0.00 \leq n_n \leq 0.60$) simultaneously prevail under the experimental cooling rates. The conformation of the $-CH_3$ group, that is, the *i*-PP backbone stereo-defect does not deflect this model-prediction. Consider particularly the 5.0 °C/min model prediction in Table 4. Here, $n_d = 3$ which indicates the formation of spherulite *i*-PP crystals. This model finding matches what Sajkiewicz et al. [72] experimentally observed for crystallization of pristine *i*-PP at the above cooling rate, using polarized light microscopy.

The crystallization profiles—α versus T relations—feature very fast primary and slow (impinged) secondary crystallizations. We shall discuss them from the perspective of Flory's equlibrium theory, particularly in terms of the level of dimensionless undercooling θ and the crystal surface free energy D, at a later section.

Figure 19 also confirms that a single E_a fits the well-known isokinetic Avrami-Erofeev crystallization mechanism throughout the entire *i*-PP crystallization process (primary plus secondary crystallization). Therefore, E_a is essentially constant of crystallization time or temperature and relative crystallinity α. Now we compare this finding with that published in the literature.

First, we consider the report by Harkin-Jones et al. [26] who modeled nonisothermal DSC crystallization of an un-nucleated *i*-PP (FINA 4060S, MFR = 3.00 g/10 min at 230.0 °C and 2.16 kg load). Note that this MFR equals to that of our experimental sample. They evaluated a number of literature models, all of which incorporate arbitrary curve-fitting parameters. The two-parameter modified Ozawa model (with induction period), extended by Hammami, Spruiell, and Mehrotra [73] performed the best.

Second, Zheng et al. [67] modeled the nonisothermal crystallization of *i*-PP (MFR = 3.88 g/10 min at 230.0 ºC and 2.16 kg load) considering an empirical nuclei density function, induction period, and temperature-dependent Hoffman–Lauritzen spherulite growth rate. This heuristic simulation model has the following limitations. It does not represent secondary crystallization for cooling rates exceeding 5.0 °C/min. It also shows that effective activation energy varies with relative crystallinity α.

Both the above curve-fitting models have unfortunately no mechanistic, kinetic, and thermodynamic basis. Hence, the model parameters and predictions, unlike those of ours, are of limited physical significance.

Third, Supaphol et al. [74] modeled the nonisothermal crystallization activation energy of selected aromatic polyesters and showed that it is a function of the relative crystallinity α. Depending on the polymer structure, it either monotonically increases, or it first increases and then it decreases as α increases. This variational trend was ascribed to the dependence of nucleation energy barrier on temperature. However, note that this explanation ignores isokinetic concept, crystal growth, as well as primary and secondary crystallizations. Hence, their model prediction and explanation are insufficient and unacceptable.

Figure 20 illustrates that the model-predicted nonisothermal crystallization frequency factor k_0 (defined by Equation 15), for the experimental *i*-PP, well correlates to the cooling rate β ($R^2 = 0.9999$). k_0 progressively increases as β increases. Our physical interpretation of this correlation follows. Considering the relation between kinetics and thermodynamics, it can be shown that $k_0 \Rightarrow \exp(S/R)$ or $S \Rightarrow R\ln k_0$ where S is entropy of the system and R is the universal gas constant. Therefore, the entropy of the experimental *i*-PP nonisothermal crystallization increases as k_0 and the cooling rate β increase. k_0 is, therefore, a measure of entropy (system disorder) and it is cooling rate-dependent. Now, we revisit the growth of crystal dimension n_d from the thermodynamic entropy perspective. Recall the results reported in Table 4. Low and increasing system disorders, among other factors, favor the growth of spherulitic and cylindrical crystals, respectively. This is a new model prediction for nonisothermal *i*-PP crystallization.

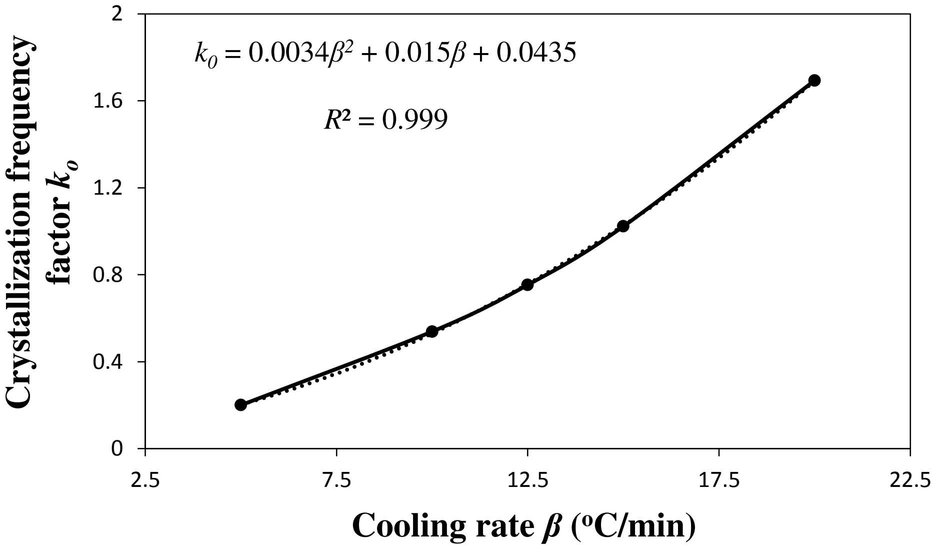

Figure 20: Effect of cooling rates on *i*-PP nonisothermal crystallization frequency factor k_o.

Figure 21 shows the effect of cooling rates on the model-predicted apparent activation energy $E_a = E_{grow} - E_{nucl}$. This is a major motif of this study. E_a does not practically vary with cooling rate β. Hence, it, unlike k_0, is entropy-independent for the experimental *i*-PP nonisothermal crystallization. This result particularly differs from what Sahay and Krishnan have reported regarding the influence of β on activation energy of aromatic polyester crystallization [75]. To fit the DSC data, these authors considered an effective activation energy E_{ea} that consists of cooling rate-independent activation energy E_0 and cooling rate-dependent activation energy E_1, which are related to each other as follows: $E_{ea} = E_0 + E_1 \ln(A\beta)$, where A is an arbitrary constant. Regrettably, this treatment, like the model by Hammami, Spruiell, and Mehrotra [73] has no mechanistic, kinetic, and thermodynamic basis. This is a purely data-fitting approach. Hence, the above effective

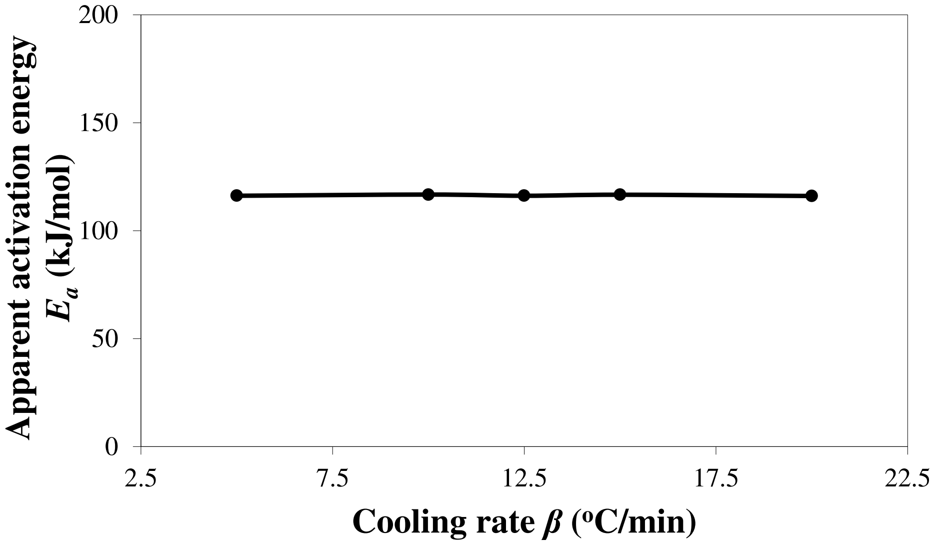

Figure 21: Effect of cooling rates on *i*-PP nonisothermal crystallization apparent activation energy E_a.

crystallization activation energy concept cannot be accepted. By contrast, our model duly considers isokinetic concept, crystal growth, as well as primary and secondary *i*-PP crystallizations; and mathematically shows that the activation energy is temperature-, entropy-, and cooling rate-independent. The pendant $-CH_3$ (methyl) group of *i*-PP, with that of the stereo-defect, despite being inclusive in the crystal lamella [39,46,51] , does not affect the invariance of E_a. Figure 22 shows the qualitative stereo-defect distribution (SDD) of the experimental *i*-PP. This was determined using Crystaf and following the procedure reported in the literature [57]. The SDD is segregated mainly into the following two regions:

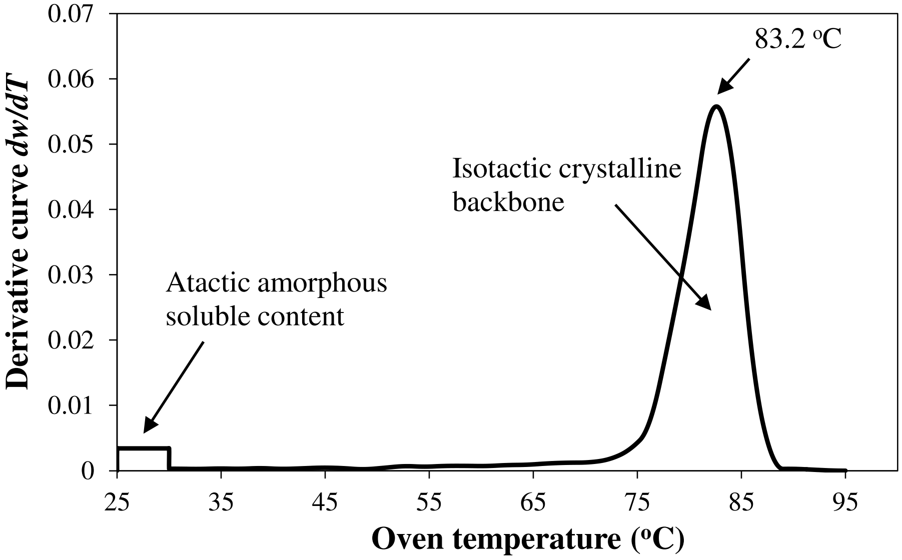

Figure 22: Crystaf analysis of the experimental Ziegler-Natta *i*-PP.

(i) the defect-rich atactic (amorphous) soluble content (4.0 wt%), and (ii) defect-lean highly isotactic crystalline backbones (around peak crystallization temperature of 83.2 °C in TCB). The interference of the former into the melt crystallization of the latter, as per the model prediction, does not affect E_a either. The overall discrete meso-pentad distributions listed in Table 5 complement Figure 22. They were determined using ^{13}C NMR spectroscopy [76,77].

Table 5: Mole fraction of configurational meso-pentad sequences in the experimental *i*-PP.

Configurational meso-pentad sequences		**Chemical shift (in ppm)**	**Mole fractions**
mmmm	*mm*-centered	21.75	0.855*
mmmr	*mm*-centered	21.56	0.028
rmmr	*mm*-centered	21.31	0.004
mmrr	*mr*-centered	20.02	0.032
mmrm + rmrr	*mr*-centered	20.87	0.016
rmrm	*mr*-centered	20.72	0.013
rrrr	*rr*-centered	20.35	0.011
mrrr	*rr*-centered	20.22	0.014
mrrm	*rr*-centered	19.92	0.027

$$MSL\text{ (meso-pentad sequence length)} = \frac{mmmm + \frac{3}{2}mrrr + 2\,rmmr + \frac{1}{2}rmrm + \frac{1}{2}rmrr}{\frac{1}{2}mmmr + rmmr + \frac{1}{2}rmrm + \frac{1}{2}rmrr} = 31.$$

The signals of *mmrm* and *rmrr* pentads overlap in the spectrum; hence, the sum (*mmrm + rmrr*) is obtained. To calculate *MSL*, the contribution of *rmrr* has been taken equal to that of *rmrr* [77]. *MSL* is also called average isotactic sequence length. $^*X_{mmmm} = 0.855$.

Based on the overall findings of Figures 19 and 21, this study confirms the invariance of activation energy articulated by Galwey and co-thinkers [78,79], and does not support the concept of variable instantaneous activation [70,73–75,80,81] which is practiced in analyzing nonisothermal crystallization kinetic data. This conclusion originates from the correct application of isokinetic concept and the current nonisothermal Avrami-Erofeev crystallization model, and the appropriate calculation algorithm that we developed. This is how we address in this study the mathematical artefact that exists in the literature.

Based on the preceding discussion, we conclude that the nonisothermal primary and secondary crystallizations of the experimental *i*-PP occur isokinetically with constant (temperature-, entropy-, and cooling rate-invariant) apparent kinetic energy. The crystal dimension varies between cylinder and sphere while instantaneous (athermal/ heterogeneous) and sporadic (thermal/homogeneous) nucleations can co-occur.

4.2 Melting behavior and crystallization of *i*-PP: Flory's equilibrium theory perspective

In this section, we discuss the melting behavior and crystallization of the experimental *i*-PP from Flory's equilibrium theory perspective, particularly considering the following three temperature-dependent dimensionless factors—critical stable crystallite sequence number n^*, level of undercooling θ, and crystal surface free energy D. See Equations 24, 25, and 26, respectively.

First, we evaluate the influence of the level of undercooling θ and crystal surface free energy D on the nonisothermal crystallization of *i*-PP. θ and D were calculated using Equations 25 and 26, respectively, and the Cycle 2 DSC data. Figure 23 demonstrates that for a given cooling rate β and beyond induction/nucleation regime ($\alpha = 0.1$), increasing θ sharply enhances the primary crystallization profile, and makes it proceed very fast. The plots shift rightward with the increase in β. Here, for a given value of the relative crystallinity (degree of crystallization) α, θ increases as β increases, without changing the apparent crystallization energy E_a. Also, see Figure 21. On the other hand, the slower secondary crystallization (impingement of crystal growth) shows milder impact of θ on α; α gradually increases with the increase in θ. This finding differs from what we notice to happen in primary crystallization. The values of θ that correspond to the onset of primary and secondary crystallizations increase with the increase in β.

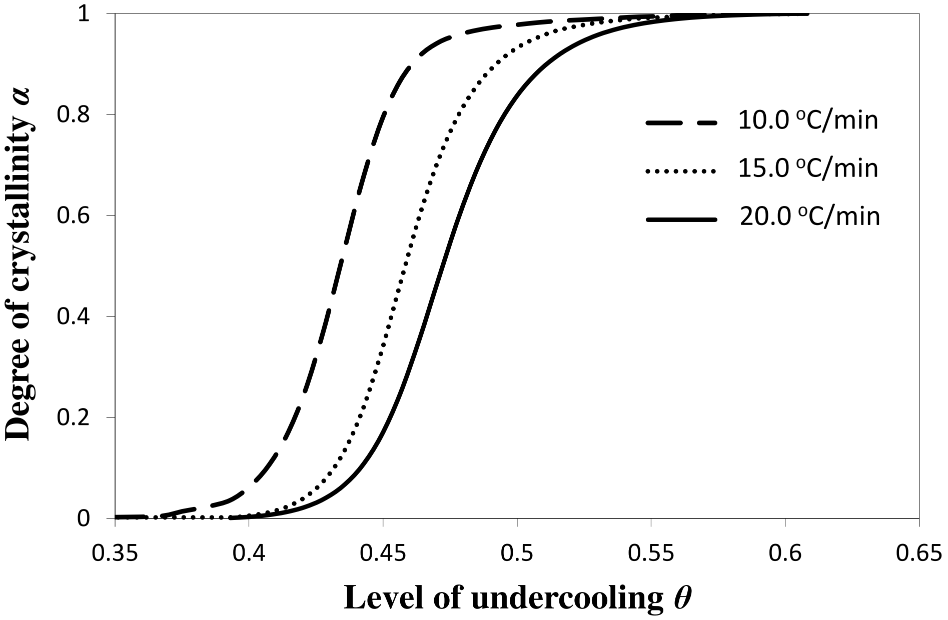

Figure 23: Variation of relative crystallinity α with level of undercooling θ.

Figure 24 investigates how crystal surface free energy D affects the nonisothermal crystallization of *i*-PP. The overall impact is opposite to that of the level of undercooling θ on relative crystallinity α. This is elaborated as follows. Here, a decrease in D rapidly accelerates the primary crystallization α. The plots shift leftward with the increase in the cooling rate β. For the same α, D decreases as β increases, without affecting E_a. On the contrary, during the slower secondary crystallization, α very gradually increases with the decrease in *D*. This trend deflects from the situation that prevails in primary crystallization. The onset secondary crystallization *D* decreases with the increase in β.

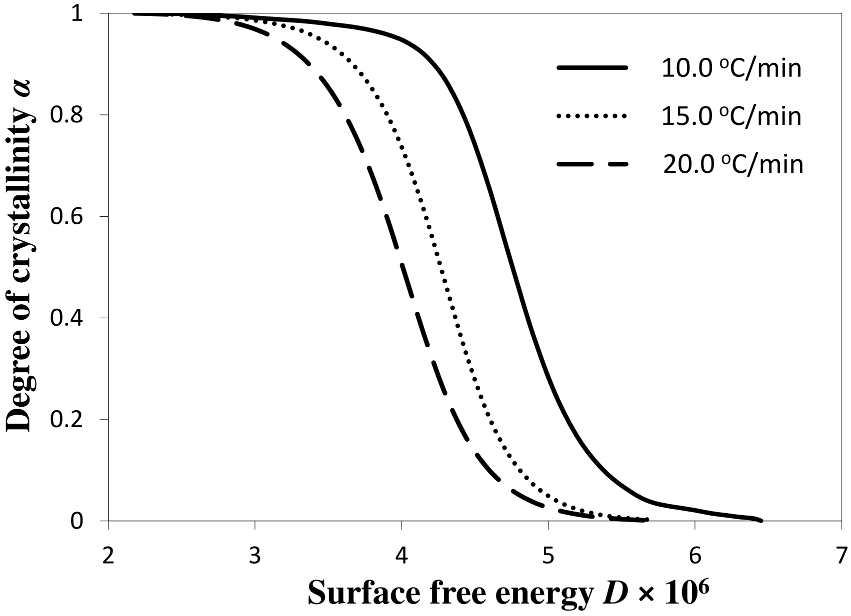

Figure 24: Variation of relative crystallinity α with dimensionless crystal surface free energy *D*.

From the above overall findings of Figures 23 and 24, we conclude that primary and secondary crystallizations originate from the increase and decrease in the level of undercooling and crystal surface free energy, respectively. In primary crystallization, the $d\alpha/d\theta$ and $-d\alpha/dD$ are much higher than the corresponding derivatives in secondary crystallization. However, these two competitive temperature-dependent equilibrium theory parameters (θ and *D*), despite having opposite variational trend, do not change the apparent crystallization energy E_a, either as a function of cooling temperature or rate. To the best of our knowledge, these are insightful new explanations for the observed characteristics of the fairly fast nonisothermal primary crystallization and very slow secondary crystallization of *i*-PP.

Figure 25 is the consequence of the combined effect of the level of undercooling θ and crystal surface free energy *D*, expressed in terms of critical (limiting) sequence number

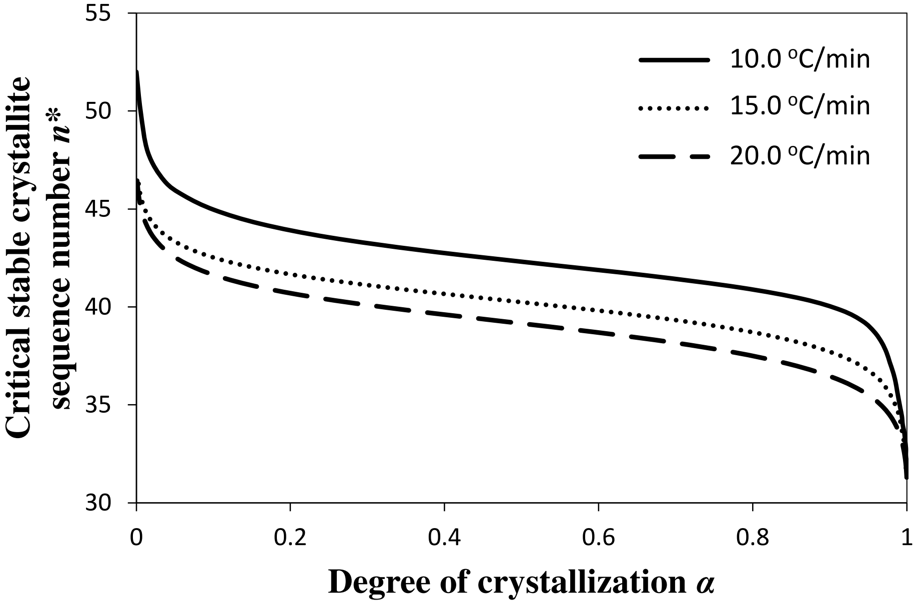

Figure 25: Variation of critical crystallite sequence number n^* with relative crystallinity α.

n^*, on the nonisothermal crystallization of *i*-PP. See Equation 3; $X_{mmmm} = 0.855$ (^{13}C NMR value); *MSL* (meso sequence length) = 31 (Table 5). $X_{mmmm} = 0.855$ fairly matches the value that $T_m = 161.0$ °C, the melting point of our experimental *i*-PP, reads from Figure 21 of Zhang et al. [2016] [82]. Note that n^* signifies the sequence of the *i*-PP repeat unit $–[CH_2–CH(CH_3)]–$ of the stable crystallite, that equilibrates with the melt at a given melt temperature. Hence, it measures the temperature-dependent dynamic critical crystallite stability. This figure shows how n^* varies as a function of α with the progressive development of the crystallinity profile. For a given cooling rate β and beyond induction/nucleation regime ($\alpha = 0.1$), n^* fairly decreases as α sharply increases during primary crystallization. Here, for a given value of α, n^* increases with the decrease in cooling rate β. During secondary crystallization, n^* steeply decreases as α slowly increases. All the plots shift rightward with the decrease in β. The n^* versus α functional variation does not affect the apparent crystallization energy E_a.

Figure 26 compares the profiles of DSC-determined temperature-dependent instantaneous (dynamic) crystallinity $\chi(T)$ for different cooling rates. $\chi(T)$ was estimated using the following relation:

$$\chi(T) = \frac{\Delta H(T)}{\Delta H_f^0} = \frac{\int_{T_i}^{T} \left(\frac{dH}{dT} \right) dT}{\Delta H_f^0} \qquad (32)$$

where ΔH_f^o is the heat of fusion (8786.4 J/mol = 207 J/g) of the perfect *i*-PP crystal (of infinite lamellar thickness and molar mass). Therefore, $\chi(T)$, unlike relative crystallinity $\alpha(T)$, is heat of fusion-based crystallinity that concerns the phases of the material solidified from the cooling melt.

The Cycle 2 DSC crystallization data were applied to calculate $\chi(T)$. For each cooling rate β, the χ versus T relation shows the following common trend. χ initially increases fairly sharply as T decreases with continued cooling. However, below a critical cooling temperature $T_{c,\,critical}$, it asymptotically flattens (which indicates hindrance (impingement) to the further development of crystallinity), and is not any further affected by decreasing T

and hence, the level of undercooling θ and crystal surface free energy D. At $T < T_{c,\ critical}$, defect-rich *i*-PP chains, having slower melt chain dynamics, crystallize [38]. $T_{c,\ critical}$ decreases with the increase in β. Only above $T_{c,\ critical}$, the following happens:

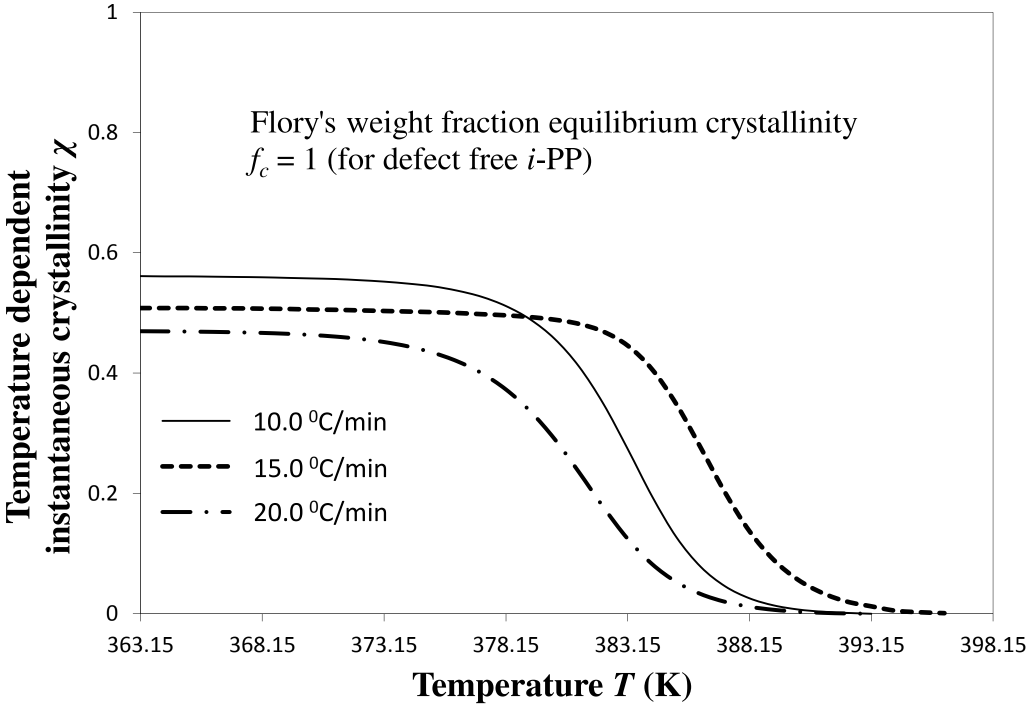

Figure 26: Variation of temperature-dependent instantaneous Cycle 2 crystallinity χ with cooling temperature.

i. χ shows to be temperature-dependent; and
ii. $\chi(T)$ increases as θ increases, and D and critical stable crystallite sequence number n^* decrease with the decrease in T.

The asymptotic value of χ equals to the Cycle 2 DSC %crystallinity of the *i*-PP sample. χ (asymptotic or non-asymptotic), for a given cooling rate, is always much less than Flory's weight fraction equilibrium crystallinity f_c, which for a defect-free *i*-PP homopolymer is equal to unity. See Equation 27 and the text below it. The predicted crystallinity difference (with respect to $f_c = 1$) may be attributed to the topology and the eventual kinetic restraint with reference to Flory's equilibrium theory [38,83–86]. Therefore, crystallinity may be improved by decreasing the kinetic and topological restraints. By topology, we mean the crystallizable isotactic polypropylene sequence length distribution SLD (due to stereo-defects), the density of chain entanglement, and the configuration of the folding lamellae. Note that according to the equilibrium theory, only sequences exceeding a certain critical length crystallize. The SLD reduces the exceedingly long sequences required for equilibrium. On the other hand, the resulting kinetic constraint imposes hindrance to nucleation and crystal growth, and impinges the growing centers. The crystallization of particularly the very long sequences becomes especially difficult. Consequently, the experimental *i*-PP does not achieve the structural topology stipulated by the equilibrium requirements, and its melting point, heat of fusion, and crystallinity decrease.

Here, we address the effects of the level of undercooling θ and crystal surface free energy D on the melting behavior of *i*-PP. See Figure 27. θ and D were calculated using Equations 25 and 26, respectively, and the Cycle 3 DSC melting data. The lamellar thickness L of folded chain crystal (FCC) of the experimental Z–N *i*-PP—a random stereo-copolymer [44–46] with configurational defects along the backbone—was calculated using the following version of Gibbs-Thompson thermodynamic equation [41,47–50]:

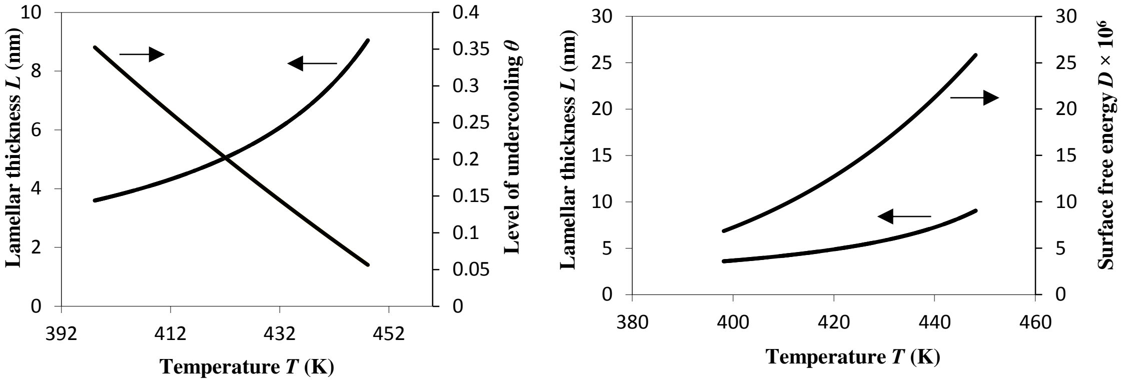

Figure 27: Variation of lamellar thickness *L*, level of undercooling θ, and crystal surface free energy *D* as a function of cooling temperature. Plots for all the experimental heating rates overlapped.

As per Flory's thermodynamic equilibrium theory, melting and crystallization are both reversible. This figure shows that melting first starts with the smaller defect-rich

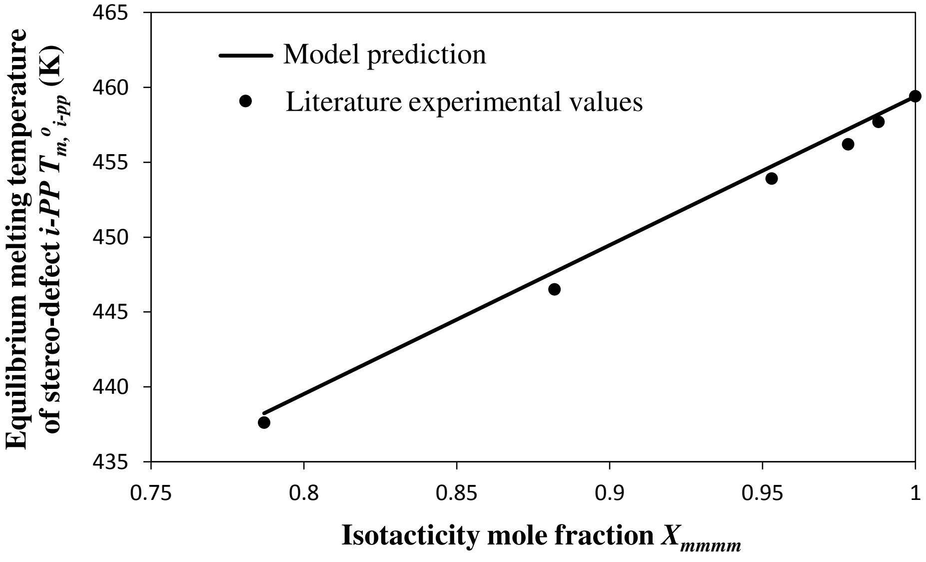

Figure 28: Comparison of the thermodynamic model-predicted equilibrium melting temperature of an *i*-PP (with stereo-defects) with that published in the literature.

lamella at lower temperatures, and higher undercooling favors this. On the other hand, the larger defect-free lamellae melt later at higher temperatures, which occurs due to lower level of undercoling θ. In either case, the lamella melting temperature is always less than the equilibrium melting temperature T_m^o of the perfect crystalline *i*-PP (459.1 K). Compare Figure 27 observation with that of Figure 22. However, the effect of crystal surface free energy D on melting behavior of *i*-PP differs from that of θ. Here, D, unlike θ, increases as the melting temperature increases, and consequently the smaller to larger lamellae sequentially melt. In summary, lamellar thickening occurs with the decrease of θ, and increase of melting temperature and D. This phenomenon significantly increases in the molten mobile phase. The *chain sliding diffusion theory* proposed by Hikosaka et al. [87–89], combined with the above variation of θ and D support this lamellar thickening behavior. The heating rate does not affect this phenomenon. These are insightful findings, and to the best of our knowledge, have not been reported earlier in the literature.

Overall, θ and D inversely influence the *i*-PP melting phenomenon. This can be explained as follows. Equation 25 shows that θ linearly increases as a function of $\frac{\Delta T}{T}$ (where $\Delta T = T_m^0 - T$), and it mathematically expresses the undercooling profile of the experimental *i*-PP with reference to the polypropylene perfect crystal (having infinite MW and lamellar thickness, and $\theta = 0$). Hence, it eventually shows the temperature gradient effect on *i*-PP melting. On the other hand, D decreases exponentially as a function of non-dimensional crystal surface free energy $\frac{\sigma_e a_o}{RT}$. See Equation 26. The above variational trends of θ and D are fundamentally related to the topologies of the lamellae and crystallite surface, which are affected by the architecture of the *i*-PP backbones.

Figure 29 illustrates that the lamellar thickness L of the experimental *i*-PP crystal shows a distribution during melting. We calculated this lamellar thickness distribution (LTD) as follows. L was estimated using Equations 28 and 29, and the corresponding mass fraction m_{T_j} (at a given temperature T_j), by applying Equation 31 and the Cycle 3 DSC data:

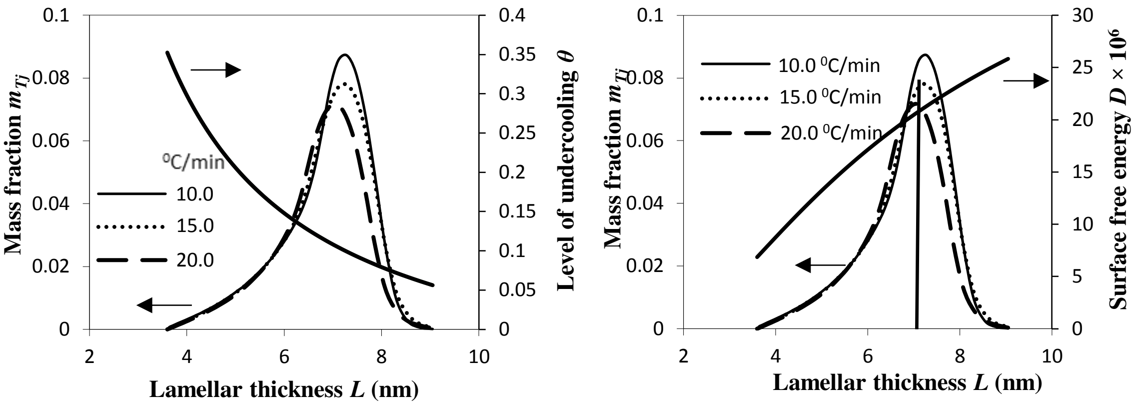

Figure 29: Variation of mass fraction of crystal lamellae melted, level of undercooling θ, and crystal surface free energy D as a function of lamellar thickness L

The above figure also demonstrates the relation that exists among the LTD, the level of undercooling θ, and crystal surface free energy D. The LTD plots particularly show that a substantial mass fraction of the crystal lamellae melts at lower θ and higher D. See the LTD at the right side of the vertical line. Also, the most probable lamellar thickness L_{MP}, melting temperature T_{MP}, level of undercooling θ_{MP}, and crystal surface free energy D_{MP}

are found to be a weak function of cooling rate β. See Table 3. All these most probable properties, for a given β, that correspond to the maximum mass fraction of the LTD, show lower θ and higher D.

4.3 Conclusions

Isotactic polypropylene (*i*-PP) is a highly important polyolefin thermoplastic that fabricates multitude of end-products. Melting and crystallization are integral parts of this fabrication process. Therefore, this report revisits the nonisothermal crystallization kinetics and melt behavior of a commercial Ziegler-Natta *i*-PP by integrating a new nonisothermal crystallization model (which we published in 2013), Flory's thermodynamic equilibrium theory, Gibbs-Thompson equation, and nonisothermal DSC experiments. Flory's equilibrium theory has been applied by considering that an *i*-PP can be microstructurally defined to be a random stereo-copolymer having configurational defects along the backbone. By applying the above simple conceptual integration, the relative crystallinity α, temperature-dependent instantaneous crystallinity χ, the crystallization kinetic triplet, and lamellar thickness and melting temperature have been duly correlated, as appropriate, to the following dimensionless factors—level of undercooling θ, crystal surface free energy D, and critical stable crystallite sequence number n^*. Consequently, new insightful results, interpretations, and explanations have been concluded. In particular, the following can be listed:

- The nonisothermal primary and secondary crystallizations of *i*-PP occur isokinetically with constant (temperature-, entropy-, and cooling rate-invariant) apparent kinetic energy E_a, which is also unaffected by the level of undercooling θ, crystal surface free energy D, and the lamella-inclusive pendant $-CH_3$ group of the i-PP repeat unit. The crystal dimension n_d varies, independent of θ and D, from cylinder to sphere. Low and high system disorder (entropy), among other factors, favor the growth of spherulitic and cylindrical crystals, respectively. Instantaneous (athermal/heterogeneous) and sporadic (thermal/homogeneous) nucleation processes may co-occur.

- The very rapid primary and slow secondary crystallizations originate from the increase and decrease in the level of undercooling θ and crystal surface free energy D, respectively. In primary crystallization, the $d\alpha/d\theta$ and $-d\alpha/dD$ are much higher than the corresponding derivatives in secondary crystallization. Despite having inverse characteristics, θ and D, do not change E_a, either as a function of cooling temperature T or rate β.
- The temperature-dependent instantaneous (dynamic) crystallinity $\chi(T)$ increases as the level of undercooling θ increases, and crystal surface free energy D decreases with the decrease in T till an asymptotic value is reached.

- Smaller lamellae first melt at lower temperatures and higher level of undercooling θ. The reverse applies to the larger lamellae. The overall lamella melting temperature is always below the equilibrium melting temperature i-PP (459.1 K). The crystal surface free energy D, unlike θ, increases as the melting temperature increases, and consequently the smaller to larger lamellae sequentially melt. A substantial mass fraction of the lamella melts at lower θ and higher D.

- Lamellar thickening occurs with the decrease of θ, and increase of melting temperature, and D. This phenomenon significantly increases in the molten mobile phase. The *chain sliding diffusion theory* proposed by Hikosaka et al. [87–89], combined with the above variation of θ and D support this lamellar thickening behavior.

The approach of this study also applies to evaluate the influence of catalyst structure, backbone defect types, and their distribution on the crystallization and melt behavior of *i*-PP.

CHAPTER 5

Nonisothermal crystallization and melt behavior of *i*-PP/graphene nanocomposites

5.1 Nonisothermal crystallization of *i*-PP/graphene nanocomposites

Polypropylene nanocomposites consisting of various carbon nanofillers are of high industrial importance. Therefore, this is a very active research subject. The widely used nanofillers, in this context, include graphite, single and multi-walled carbon nanotubes (SWCNTs and MWCNTs), and graphene oxide (GO) [90–98]. Novoselov, Geim, and coworkers discovered graphene—the world's thinnest material—in 2004. Graphene comprises a single layer of graphite having a two dimensional sheet of sp^2 carbon atoms which are arranged in a honeycomb structure [99]. This unique structure imparts several outstanding properties to it, such as immensely high thermal conductivity, Young's modulus, and electrical conductivity [100–104]. This is why, it shows immense potential to replace the traditional fillers. Graphene-based nanocomposites have been reported to be used in electronics, sensors and actuators, solar cells and data storage, optics and photonics, medical and biological applications, tissue engineering, and biomaterials [105].

The fabrication of *i*-PP–graphene nanocomposite end-products involves heating and cooling during processing. It melts and crystallizes upon heating and cooling, respectively. These phenomena affect the nanocomposite structure which controls the properties and applications listed above. Practical fabrication processes such as injection molding, extrusion molding, extrusion blow molding, and vacuum forming mostly undergo non-isothermal crystallization. Hence, it is very important to investigate *i*-PP−graphene nanocomposite nonisothermal crystallization, particularly the kinetics, and melting behavior to generate knowledge that can be used to efficiently operate industrial fabrication processes and manufacture end-products with better properties and improved performance [26,67,72,106–108].

The overall published work, in the present context, concerning crystallization and melting behavior refers to the following different nanocomposites: (i) *i*-PP−CNT [90,92,96–98]; (ii) *i*-PP−montmorillonite [65] and *i*-PP−calcium carbonate [64]; (iii) *i*-PP−exfoliated graphite [91,94]; and (iv) *i*-PP−graphene (GNP) [93,100,101,103–105,109]. Our focus, as indicated above, is on *i*-PP−GNP nanocomposite without using any nucleating agent. Therefore, we summarize the major finding in this particular area. GNP increases crystallization rate. This has been explained by stating that it acts as a nucleating agent by increasing the nucleation sites and decreasing the nucleation induction period. The limitations of the published *i*-PP−GNP nanocomposite research are summarized below.

The above studies investigated crystallization kinetics using Caze-Chuah, Jeziorny, Ozawa, Mo, and Seo-Kim models (as appropriate) [65,96,97,110–113]. However, these models are not mechanistic; they are empirical; and they lack fundamental and phenomenological formalism. The model parameters do not always have adequate physical significance. Some of them do not represent the entire crystallization profile, and some experience double logarithm insensitivity and linearization problems. See Reference [114] for the details.

We also observe that the aforementioned reports did not study the *i*-PP−GNP nanocomposite dynamic melting behavior (including lamellar thickening) and crystallization from Flory's equilibrium theory perspective, particularly considering the following three temperature-dependent dimensionless factors—level of undercooling θ, crystal surface free energy D, and critical stable crystallite sequence number n^*. Therefore, we integrate the fundamental mechanistic crystallization model (which we published in 2013) [114], Flory's thermodynamic equilibrium theory [38,115,116], Gibbs-Thompson equation [41,48–50,117], and DSC experiments, aiming at generating new and/or better insightful results, interpretations, and explanations regarding nonisothermal *i*-PP−GNP nanocomposite crystallization and melt process. Note that such an integrated conceptual framework to study the subject thermal behavior, as far as we know, has not been yet published. Therefore, we undertake this study.

The merits of our above crystallization model over the other literature models are well documented [52,114,118,119]. This is based on mechanistic consideration. It applies to the entire DSC nonisothermal crystallization curve. The model-predicted kinetic parameters—apparent kinetic energy E_a, Avrami exponent n, and crystallization frequency factor k_0—have physical significance.

We also plan to pursue the above objective by correlating the relative crystallinity α, temperature-dependent instantaneous crystallinity χ, E_a, crystal dimension n_d, nucleation mode n_c, k_0, and the lamellar thickness and melting temperature, as appropriate, to θ, D, and n^*. The DSC experiments, as a function of GNP wt%, will be conducted using an *alpha*-phase commercial Ziegler-Natta *i*-PP without adding any standard nucleating agent.

The results obtained from DSC, GPC, results of lamellar thickness distribution parameters *i*-PP and *i*-PP/GNP nanocomposites are summarized in Table 6 below.

Table 6: Summary of the experimental *i*-PP and *i*-PP/GNP nanocomposite properties.

Properties	*i*-PP/GNP nanocomposite wt%					
	0.0	**0.1**	**0.5**	**1.0**	**2.0**	**3.0**
Peak melting point T_{pm} (°C)	160.9	161.5	162.1	161.9	162.4	162.4
Peak crystallization point T_{pc} (°C)	117.1	121.2	122.9	124.2	124.7	125.3
Crystallinity χ_c (%) 3rd cycle	45.15	49.71	46.85	46.51	48.85	47.57
Crystallinity χ_c (%) 2nd cycle	54.53	57.07	57.78	59.53	58.54	56.06
i-PP material density ρ_{poly} (g/cm^3)	0.892	0.897	0.894	0.894	0.896	0.895
Amorphous volume fraction ϕ_a	0.576	0.531	0.559	0.562	0.539	0.552
Weight average lamellar thickness $L_{WAV\ DSC\ GT}$ (nm)	5.59	5.61	5.62	5.60	5.63	5.58
Most probable lamellar thickness $L_{MP\ DSC\ GT}$ (nm)	5.91	5.89	5.88	5.92	5.91	5.89
Variance of LTD σ_{LTD} (nm)	2.49	2.51	2.50	2.52	2.48	2.51

Figure 30 compares the model-predicted relative crystallization profiles, determined using Equation 11, with the corresponding DSC profiles for different GNP compositions. The agreement between model and experiment, in each case, is excellent. The crystallization profiles gradually shifted rightward with the increase in GNP wt%. We notice that a single kinetic triplet (n, k_0, and E_a), for a given GNP wt%, represents the whole crystallization regime (primary as well as secondary); crystallization temperature does not change this. Therefore, the same mechanisms of nucleation and crystal growth operate all throughout the crystallization process. This remark holds for the pristine *i*-PP as well as the *i*-PP/GNP nanocomposites. This is how the present model overcomes the drawbacks and limitations of the arbitrary parameter-based existing nonisothermal crystallization models reported in the literature [26,114]. Hence, the assumption of variable crystallization mechanism, selectively reported in the literature [26,69,70,120,121], does not hold.

Now, we evaluate the effect of GNP on the relative rates of nucleation and crystal growth as follows.

Using Equations 14 to 17, we can drive the following relation:

$$\frac{1}{C}\frac{k_{nucl,0}}{k_{grow,0}} = \left[\frac{1}{k_0}\exp\left(\frac{E_a}{RT_0}\right)\right] \times \exp\left(-\frac{E_a}{RT}\right) \quad where\ C = \frac{k_s N_0}{V_0} \tag{33}$$

We expand $\exp\left(-\frac{E_a}{RT}\right)$ of Equation 33, according to Taylor series, as:

$$\exp\left(-\frac{E_a}{RT}\right) = 1 - \frac{E_a}{RT} + \frac{1}{2!}\left(\frac{E_a}{RT}\right)^2 - \frac{1}{3!}\left(\frac{E_a}{RT}\right)^3 + \dots\dots\dots\dots\dots\dots\dots \tag{34}$$

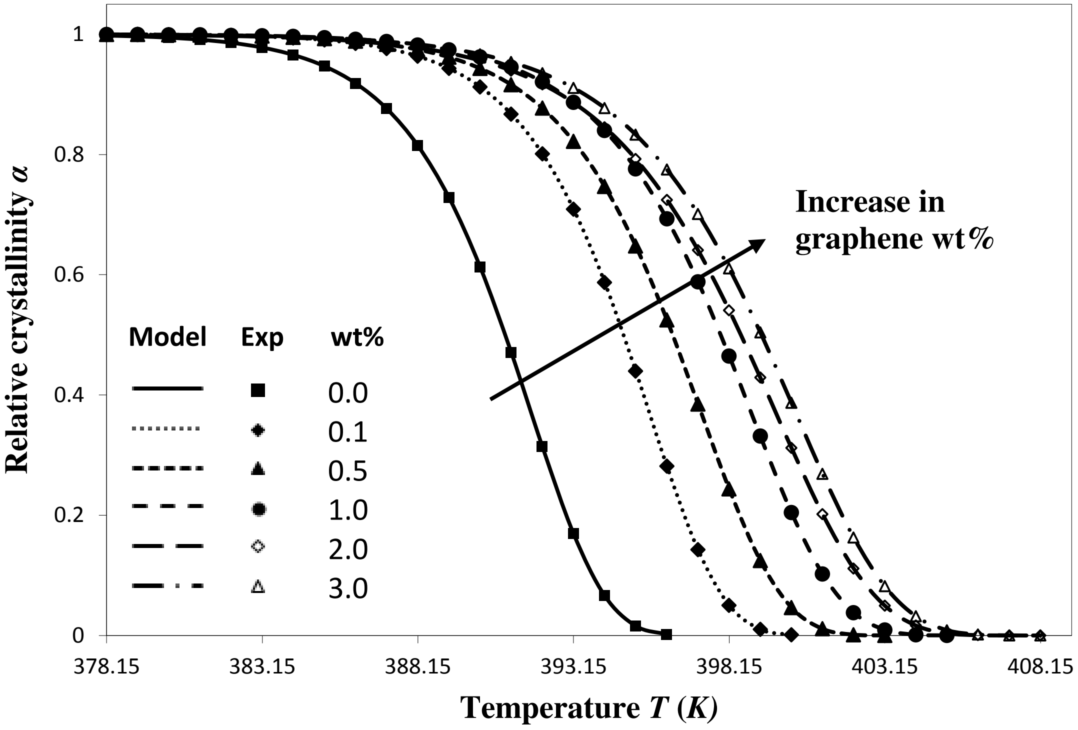

Figure 30: Comparison of model-predicted relative crystallization profiles of pristine *i*-PP and *i*-PP/graphene nanocomposites with those determined using DSC experiments.

We calculated $\frac{E_a}{RT}$, for *i*-PP and *i*-PP–GNP nanocomposites, using the present crystallization model-predicted E_a and the Cycle 2 DSC data. We found the following: $0.03535 \leq \frac{E_a}{RT} \leq 0.04287$; hence, $\frac{E_a}{RT} << 1$. So, Equation 34 can be written as $\exp\left(-\frac{E_a}{RT}\right) = 1 - \frac{E_a}{RT} \approx 1$. This reduces Equation 33 to $\frac{1}{C}\frac{k_{nucl,0}}{k_{grow,0}} = \frac{1}{k_0}\exp\left(\frac{E_a}{RT_0}\right) \neq f(T, \theta, and\, D)$. Accordingly, we estimated $\frac{1}{C}\frac{k_{nucl,0}}{k_{grow,0}} = 2.73$ and 7.46 for *i*-PP and *i*-PP–GNP nanocomposite (3.0 wt% that corresponds to asymptotic crystallization rate), respectively. This shows that graphene increases the nucleation rate by several folds over the crystal growth rate. This is another manifest of the merit of the new crystallization model. Such a proof does not appear in the literature.

Table 7: Model-predicted crystallization kinetic parameters for *i*-PP/GNP nanocomposites.

GNP wt%	Crystallization kinetics parameters	*i*-PP/GNP nanocomposites
0.0	n k_o (min^{-1}) E_a (kJ/mol) R^2	2.75 0.25 192.78 0.9921
0.1	n k_o (min^{-1}) E_a (kJ/mol) R^2	2.90 0.14 187.67 0.9925
0.5	n k_o (min^{-1}) E_a (kJ/mol) R^2	3.10 0.14 159.28 0.9950
1.0	n k_o (min^{-1}) E_a (kJ/mol) R^2	3.40 0.14 135.45 0.9920
2.0	n k_o (min^{-1}) E_a (kJ/mol) R^2	3.70 0.16 107.99 0.9918
3.0	n k_o (min^{-1}) E_a (kJ/mol) R^2	3.70 0.15 110.61 0.9910

Table 7 shows that the model-predicted n_d, as a function of GNP wt%, spans 2 and 3. For low GNP content (up to 0.1 wt%) n_d = 2. Beyond this value, n_d = 3. Therefore, increasing GNP wt% transforms the mode of crystal growth from cylindrical to spherical. Therefore, our isokinetic crystallization model predicts the advantage of adding GNP nanofiller to *i*-PP. Exceeding a critical composition, GNP aids achieving the desired spherical morphology. Now, we address the nucleation mechanism; $0.10 \leq n_n \leq 0.90$ (according to Equation 18). Therefore, in *i*-PP and *i*-PP–GNP nanocomposites, instantaneous (athermal/heterogeneous) as well as sporadic (thermal/homogeneous) nucleations can simultaneously occur. The following factors—the *i*-PP backbone stereo-defects, lamella-inclusive $-CH_3$ group [33,37,116], and the interaction of GNP with the polymer backbone—may be ascribed to this.

The model-predicted nonisothermal crystallization frequency factor k_0 (defined by Equation 15) does not practically vary with GNP wt%. See Table 7. We interpret this result as follows. Considering the relation between kinetics and thermodynamics, it can be shown that $k_0 \Rightarrow \exp(S/R)$ or $S \Rightarrow R\ln k_0$ where S is entropy of the system and R is the universal gas constant [122]. Therefore, k_0 measures the crystallization entropy. The observed invariance of k_0 with GNP wt% reflects that GNP resists system disorder during crystallization.

Figure 31 demonstrates how GNP wt% affects average crystallization rate $(t_{1/2})^{-1}$ and the apparent activation energy E_a. The effect is two-fold and opposite. GNP increases $(t_{1/2})^{-1}$. Hence, it acts as a nucleating agent. This finding matches what has been reported in the literature [93,100,101,103–105,109]. However, the literature does not adequately explain this result. The present crystallization model, as per Figure 31, illustrates that the interaction of GNP with *i*-PP backbone decreases E_a. This finding, therefore, argues for the observed GNP nucleation behavior. We shall also explain the GNP-mediated increased crystallization rate from Flory's thermodynamic quilibrium theory in the next section.

Figure 32 expands the role that GNP plays in its composite with *i*-PP. The crystallization induction time t_{ind} decreases with GNP wt%, which again corresponds to what the literature reports [93,100,101,103–105,109]. This result is a consequence of GNP nucleation effect.

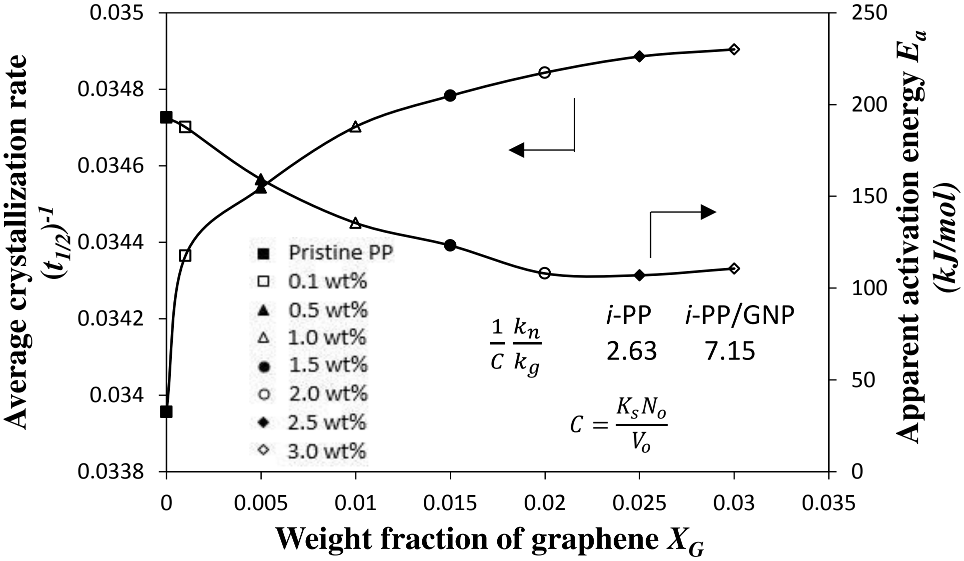

Figure 31: Effect of graphene wt% on average crystallization rate $(t_{1/2})^{-1}$ and apparent activation energy E_a.

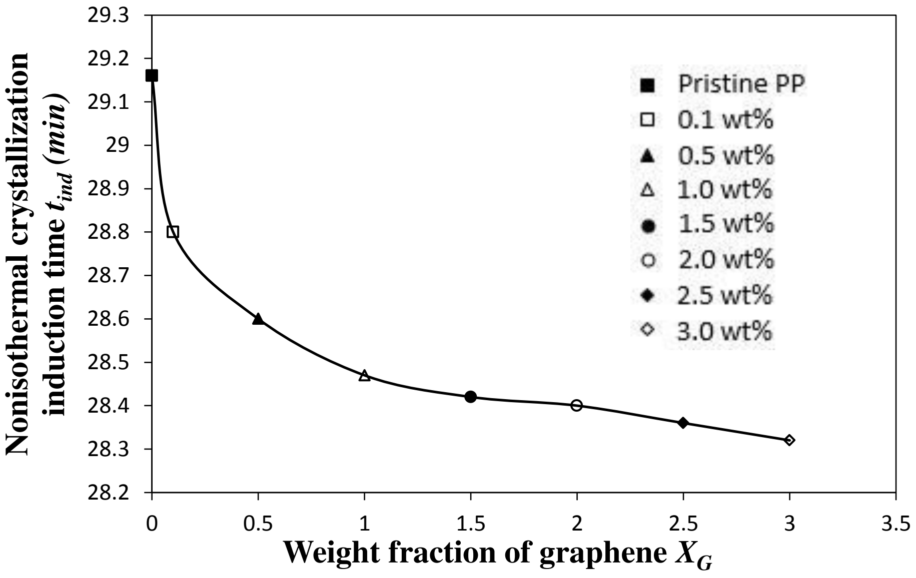

Figure 32: Effect of graphene wt% on nonisothermal crystallization induction time t_{ind} ($\alpha = 0.10$).

5.2 Nonisothermal crystallization and melt behavior of *i*-PP/graphene nanocomposites

Here, we discuss the crystallization and melting behavior of the experimental *i*-PP/GNP nanocomposites using Flory's equilibrium theory level of undercooling θ, crystal surface free energy D, and critical stable crystallite sequence number n^*. Equations 25, 26, and 24 consecutively define them. DSC Cycle 2 and Cycle 3 data were used to investigate the crystallization and melting behavior, respectively.

Figure 33 first illustrates a common effect. θ affects relative crystallinity (α) profile, with and without GNP, in a similar fashion. During primary crystallization ($0.1 \leq \alpha \leq 0.9$), $\frac{d\alpha}{d\theta}$ is quite steep while it is very low during secondary crystallization ($\alpha \geq 0.9$).

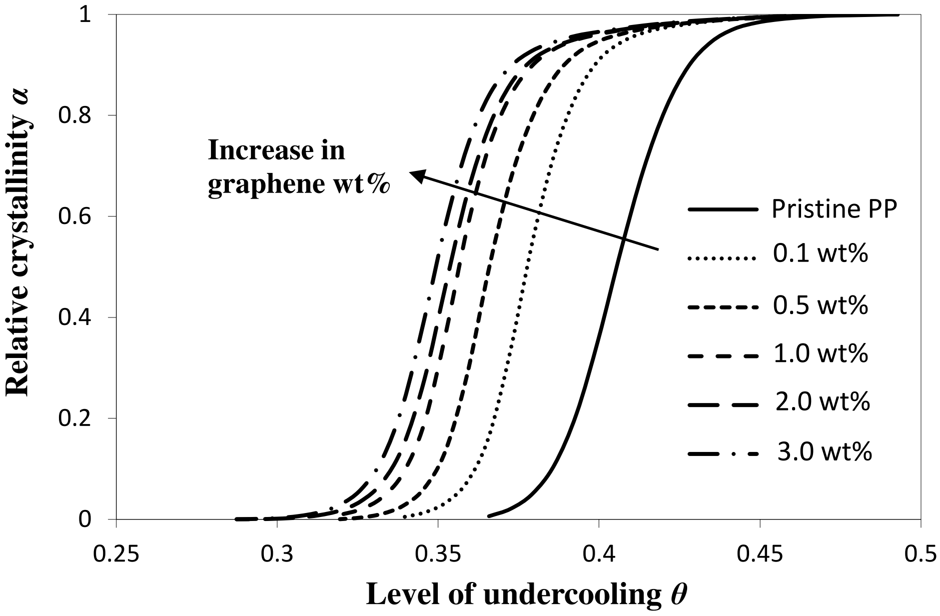

Figure 33: Variation of relative crystallinity α of pristine *i*-PP and *i*-PP/graphene nanocomposites as a function of level of undercooling θ graphene wt%.

Second, the incorporation of GNP progressively translates the α profiles toward the left. This shows that the increasing GNP wt% makes crystallization happen at lower θ region(s). Figure 34 shows the overall opposite influence of D on α. These Figure 33 and Figure 34 results, therefore, provide new explanation regarding nonisothermal crystallization of *i*-PP and i-PP–GNP nanocomposites.

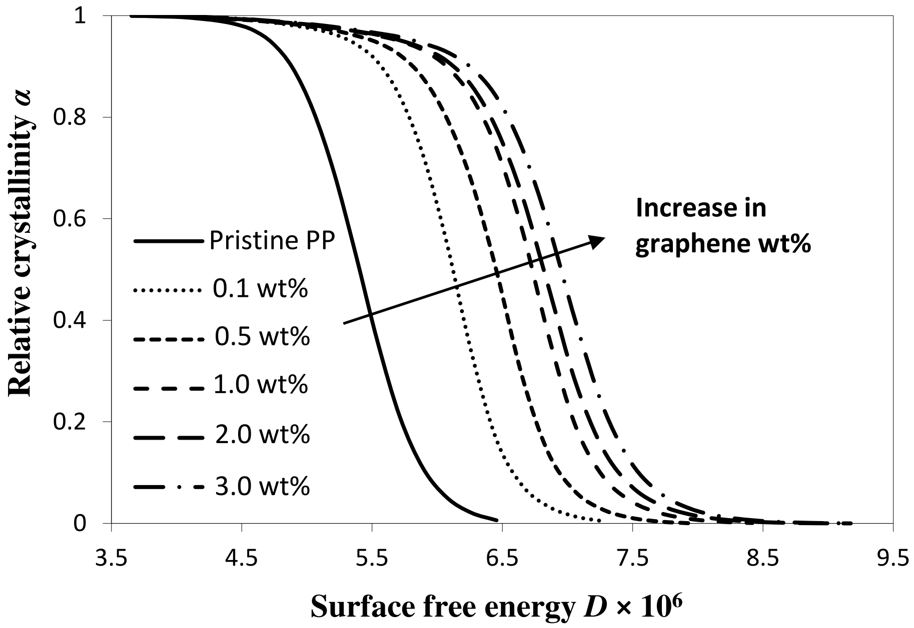

Figure 34: Variation of relative crystallinity α of pristine *i*-PP and *i*-PP/graphene nanocomposites as function of crystal surface free energy D and graphene wt%.

Figure 35 models the crystal stability phenomenon. n^* gradually decreases during primary crystallization. However, it drops much more abruptly during secondary crystallization. For a given value of α, n^* increases with GNP wt%. This is a significant conclusion. The interaction of GNP with *i*-PP backbones, hence, contributes to stabilizing the crystallite.

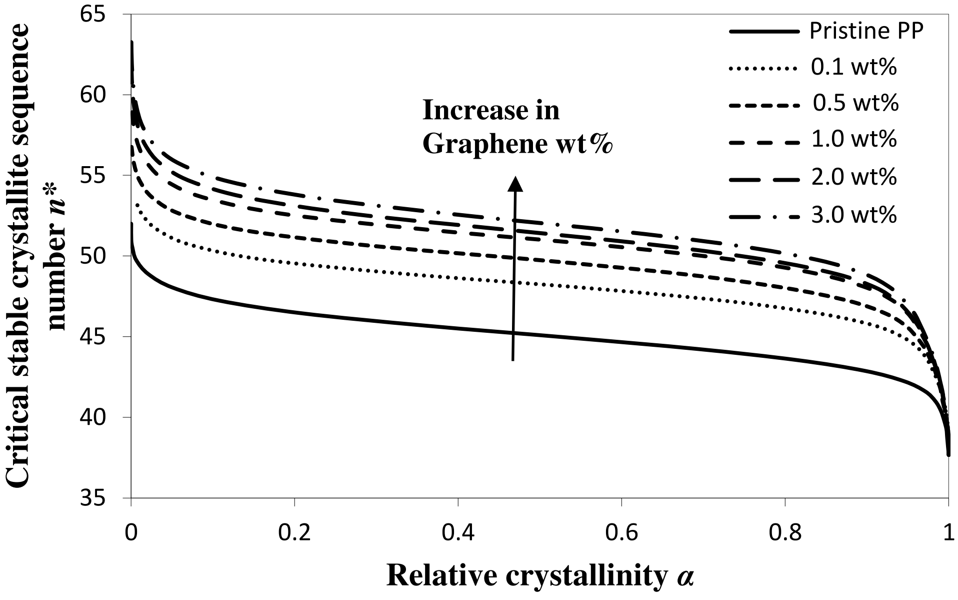

Figure 35: Variation of relative crystallinity *α* of pristine *i*-PP and *i*-PP/graphene nanocomposites as a function of critical crystallite sequence number *n** and graphene wt%.

Now, we investigate the variation of crystallization rate $(t_{1/2})^{-1}$ from Flory's equilibrium theory view point. Figures 36 and 37 vividly show that the increase in $(t_{1/2})^{-1}$, is because of decreasing θ and increasing D (due to interation of GNP with *i*-PP backbones), respectively. Also, see Figure 31 model prediction on E_a, which is another factor that explains variation of $(t_{1/2})^{-1}$. Therefore, normalized temperature gradient (with respect to equilibrium melting temperature T_m^0), crystallite surface effects, and apparent activation energy influence GNP-mediated increased crystallization rate. The Figure 33 to Figure 37 results add to the list of new insightful findings which, to the best of our knowledge, have not been so far reported in the literature.

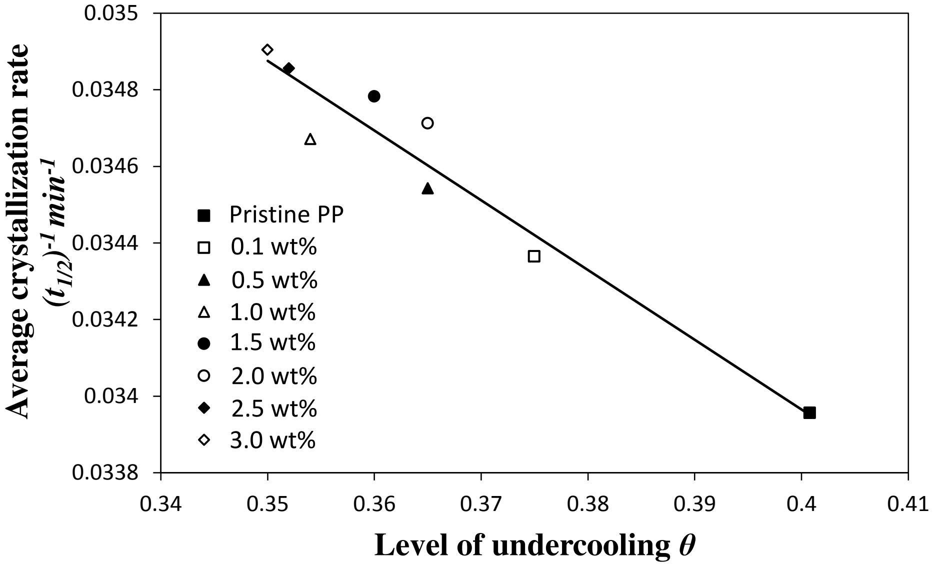

Figure 36: Variation of average crystallization rate $(t_{1/2})^{-1}$ as a function of level of undercooling θ.

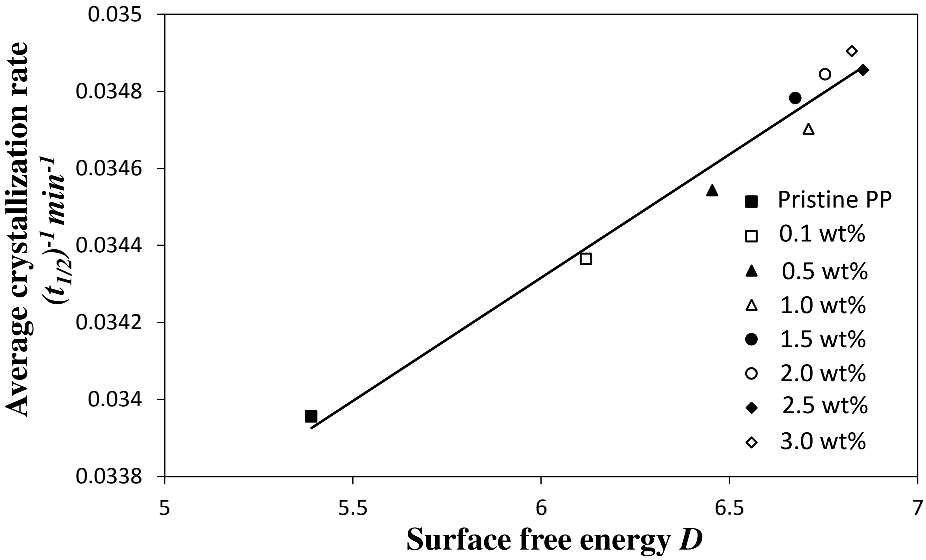

Figure 37: Variation of average crystallization rate $(t_{1/2})^{-1}$ as a function of surface free energy *D*.

Here, we address the effects of the level of undercooling θ and crystal surface free energy *D* on the melting behavior of *i*-PP and *i*-PP–GNP nanocomposite. See Figure 38, in which the lamellar thickness distribution (LTD) was calculated using Equations 30, 31, and 33; and Cycle 3 DSC melting data. GNP hardly affects LTD.

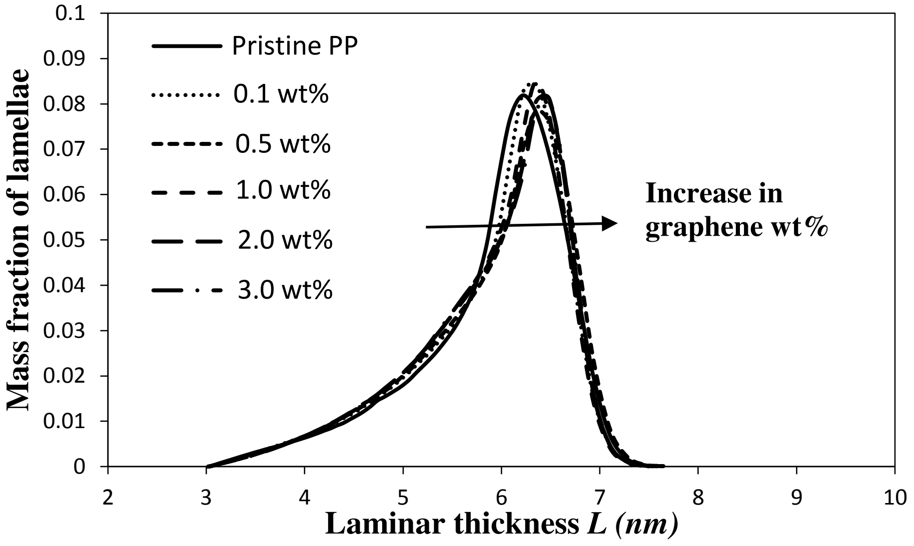

Figure 38: Effect of graphene wt% on lamellar thickness distribution *L* of pristine *i*-PP and *i*-PP/graphene nanocomposites.

As per Flory's thermodynamic equilibrium theory, melting and crystallization are reversible. Figure 39 shows that melting first starts with the smaller defect-rich lamellae at lower temperatures, and higher undercooling favors this. On the other hand, the larger defect-free lamellae melt later at higher temperatures, which occurs due to lower level of undercoling θ. In either case, the lamella melting temperature is always less than the equilibrium melting temperature T_m^o of the perfect crystalline *i*-PP (459.1 K). However, the effect of crystal surface free energy *D* on melting behavior of *i*-PP and *i*-PP–GNP nanocomposites differs from that of θ. Here, *D*, unlike θ, increases as the melting temperature increases, and consequently the smaller to larger lamellae sequentially melt. In summary, lamellar thickening occurs with the decrease of θ, and increase of melting temperature and *D*. This phenomenon significantly increases in the molten mobile phase. The *chain sliding diffusion theory* proposed by Hikosaka et al. [88,89,123], combined with the above variation of θ and D support this lamellar thickening behavior. This insightful finding remains, to the best of our knowledge, unreported in the literature.

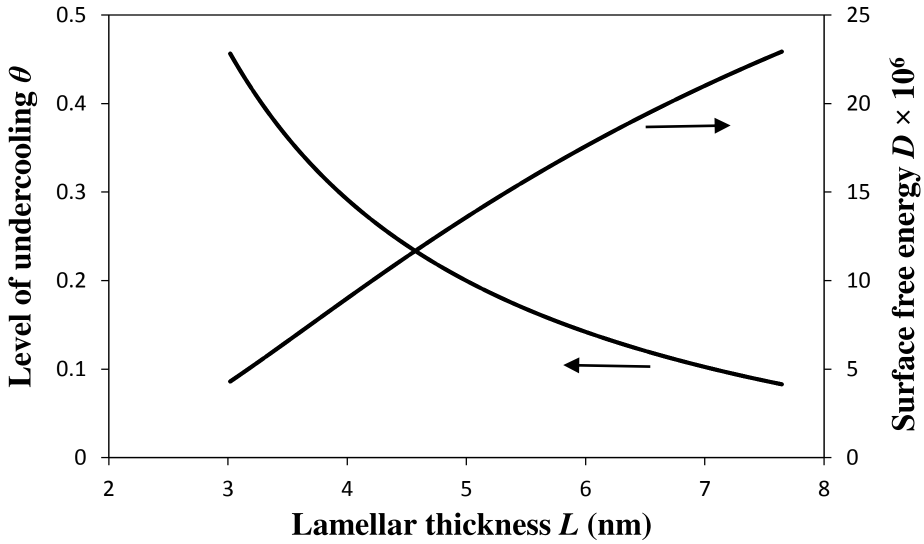

Figure 39: Effect of level of undercooling θ, surface free energy D, and graphene wt% on lamellar thickness (that is, melting process).

Overall, θ and D inversely influence the *i*-PP and *i*-PP–GNP nanocomposite melting phenomenon. This can be explained as follows. Equation 4 shows that θ linearly increases as a function of $\frac{\Delta T}{T}$ (where $\Delta T = T_m^0 - T$), and it mathematically expresses the undercooling profile of the experimental *i*-PP and the subject nanocomposites with reference to the polypropylene perfect crystal (having infinite MW and lamellar thickness, and $\theta = 0$). Hence, it eventually shows the temperature gradient effect on the above melting process. On the other hand, D decreases exponentially as a function of non-dimensional crystal surface free energy $\frac{\sigma_e a_o}{RT}$. See Equation 5. The above variational trends of θ and

D are fundamentally related to the topologies of the lamellae and crystallite surface. By topology, we mean the crystallizable isotactic polypropylene sequence length distribution SLD (due to stereo-defects), the density of chain entanglement, and the configuration of the folding lamellae.

5.3 Conclusions

Melting and crystallization are invariably involved in fabricating *i*-PP–GNP nanocomposite end-products. Hence, the crystallization and melt behavior of selected as-synthesized commercial Ziegler-Natta *i*-PP–GNP nanocomposites have been investigated by integrating a new crystallization model (which we published in 2013), Flory's thermodynamic equilibrium theory, Gibbs-Thompson equation, and nonisothermal DSC experiments. Flory's equilibrium theory has been applied by considering that an *i*-PP can be microstructurally defined to be a random stereo-copolymer having configurational defects along the backbone. The nonisothermal crystallization kinetics and melting phenomena have been related to the level of undercooling θ, crystal surface free energy D, and critical stable crystallite sequence number n^*. Consequently, new insightful results, interpretations, and explanations have been concluded. In particular, the following can be listed:

- A single kinetic triplet (n, k_0, and E_a), with invariable crystallization mechanism and system entropic disorder, represents the very rapid primary and slow secondary crystallizations. The level of undercooling θ, crystal surface free energy D, and the lamella-inclusive pendant $-CH_3$ group of the *i*-PP repeat unit do not affect the above kinetic parameters. Heterogeneous and homogeneous nucleation can co-occur. In primary crystallization, the $d\alpha/d\theta$ and $-\,d\alpha/dD$ are much higher than the corresponding derivatives in secondary crystallization.

- Graphene acts as a nucleating agent, increases the nucleation and average crystallization rates, transforms the mode of crystal growth from cylindrical to spherical, stabilizes the crystallite, and decreases the apparent crystallization energy and induction period. It causes crystallization at lower θ and higher D regions.

- Smaller defect-rich lamellae first melt at lower temperatures and higher level of undercooling θ. The reverse applies to the larger defect-free lamellae. The crystal surface free energy D, unlike θ, increases as the melting temperature increases, and consequently the smaller to larger lamellae sequentially melt.

- Lamellar thickening occurs with the decrease of θ, and increase of melting temperature, and D. This phenomenon significantly increases in the molten mobile phase. The *chain sliding diffusion theory* proposed by Hikosaka et al. [88,89,123], combined with the above variation of θ and D support this lamellar thickening behavior.

The approach of this study applies, in general, to evaluate the influence of catalyst structure, backbone defect types, and their distribution on the crystallization and melt behaviors of polyolefin/nanofiller composites.

CHAPTER 6

Recommendations for future work

The recommendations for future work are as follows:

1. Apply the present integrated concept to very fast DSC experiments
2. Revisit the crystallization and melting behavior by modeling the catalyst active center distribution, and conducting successive self-nucleation and annealing (SSA) DSC experiments
3. Study Gibb's free energy of crystallization as a function of cooling rates and graphene content
4. Investigate dynamic crystal growth
5. Conduct XRD and polarized spectroscopic investigation of crystallization

References

[1] A.V. Lavrenov, L.F. Saifulina, E.A. Buluchevskii, E.N. Bogdanets, Propylene Production Technology : Today and Tomorrow, 7 (2015) 175–187.

[2] S. Jasper and M. Mahmoud, A Techno-Economic Comparison between Two Methanol-to-Propylene Processes, Processes. 3 (2015) 684–698.

[3] A. Corma, F.V. Melo, L. Sauvanaud, F. Ortega, Light cracked naphtha processing: Controlling chemistry for maximum propylene production, Catal. Today. 107 (2005) 699–706.

[4] P.J. Beattie, Propene, in: Encycl. Toxicol. (2005) 535–536.

[5] D.B. Malpass, E.I. Band, An Overview of Industrial Polypropylene Processes, Introduction to industrial polypropylene: properties, catalysts processes. John Wiley & Sons, (2012) 183–200.

[6] D.B. Malpass and E.I. Band, The Future of Polypropylene, Introduction to industrial polypropylene: properties, catalysts processes. John Wiley & Sons, 2012

[7] D.B. Malpass, E.I. Band, Ziegler-Natta Catalysts, Introduction to industrial polypropylene: properties, catalysts processes. John Wiley & Sons, (2012) 59–74.

[8] J.C. Chadwick, G. Morini, G. Balbontin, I. Camurati, J.J.R. Heere, I. Mingozzi, F. Testoni, Effects of internal and external donors on the regio- and stereoselectivity of active species in $MgCl_2$-supported catalysts for propene polymerization, Macromol. Chem. Phys. 202 (2001) 1995–2002.

[9] L. Barino, R. Scordamaglia, Modelling of isospecific Ti sites in $MgCl_2$ supported heterogeneous Ziegler-Natta catalysts, Macromol. Theory Simul. 7 (1998) 407–419.

[10] L. Albizzati, E. Cecchin, G. Chadwick, J. C. Collina, G. Giannini, U. Morini G. Noristi, Polypropylene Handbook, 2005.

[11] P. Hermans, J. P. Henrioulle, US 4210738, Solvay (1972).

[12] Y. V. Kissin, X. Liu, D.J. Pollick, N.L. Brungard, M. Chang, Ziegler-Natta catalysts for propylene polymerization: Chemistry of reactions leading to the formation of active centers, J. Mol. Catal. A Chem. 287 (2008) 45–52.

[13] M. Chang, X. Liu, P.J. Nelson, G.R. Munzing, T.A. Gegan, Y. V. Kissin, Ziegler–Natta catalysts for propylene polymerization: Morphology and crystal structure of a fourth-generation catalyst, J. Catal. 239 (2006) 347–353.

[14] S. Kotha, Statistical Analysis of the Stereo Defect Sequence Distributions of Ziegler-Natta Isotactic Poly (Propylene) in Light of the Crystallization Behavior of Its Citref Fractions, The Florida State University, 2005.

[15] E.P. Moore, Polypropylene Handbook, Hanser Publications Inc., NY, 1996.

[16] K.S. Novoselov, A.K. Geim, S. V Morozov, D. Jiang, Y. Zhang, S. V Dubonos, I. V Grigorieva, A.A. Firsov, Electric Field Effect in Atomically Thin Carbon Films, Sci. VO, 306. (2004) 666.

[17] H. Kim, A.A. Abdala, C.W. MacOsko, Graphene/polymer nanocomposites, Macromolecules, 43 (2010) 6515–6530.

[18] C. Lee, X. Wei, J.W. Kysar, J. Hone, Measurement of the elastic properties and intrinsic strength of monolayer graphene, Science. 321 (2008) 385–388.

[19] A.A. Balandin, S. Ghosh, W. Bao, I. Calizo, D. Teweldebrhan, F. Miao, C.N. Lau, Superior thermal conductivity of single-layer graphene, Nano Lett. 8 (2008) 902–907.

[20] X. Du, I. Skachko, A. Barker, E.Y. Andrei, Approaching ballistic transport in suspended graphene, Nat. Nanotechnol. 3 (2008) 491–495.

[21] I. Atiqullah, M. Hossain, M. M. Kamal, M. S. Al-Harthi, M. A. Khan, M. J. Hossaen, A. Hussain, Crystallization kinetics of PE-b-isotactic PMMA diblock copolymer synthesized using $SiMe_2$ (Ind) $2ZrMe_2$ and MAO cocatalyst, AIChE J. 59 (2013) 200–212.

[22] M. Avrami, Kinetics of phase change. I General theory, J. Chem. Phys. 7 (1939) 1103–1112.

[23] A.T. Lorenzo, M.L. Arnal, J. Albuerne, A.J. Müller, DSC isothermal polymer crystallization kinetics measurements and the use of the Avrami equation to fit the data: guidelines to avoid common problems, Polym. Test. 26 (2007) 222–231.

[24] M. Muthukumar, Nucleation in polymer crystallization, Adv. Chem. Phys. 128 (2004) 1–64.

[25] M. Atiqullah, M.M. Hossain, S. Adamu, A. Hossaen, Thermal behaviour of polyethylene-block-poly (methyl methacrylate) block copolymer: effect of multiple heating and cooling rates versus mathematical artefact, Polym. Int. 63 (2014) 1824–1834.

[26] Y. Mubarak, E.M.A. Harkin-Jones, P.J. Martin, M. Ahmad, Modeling of non-isothermal crystallization kinetics of isotactic polypropylene, Polymer. 42 (2001) 3171–3182.

[27] L. Mandelkern, The crystalline state in physical properties of polymers, 1984.

[28] P.J. Flory, Principles of polymer chemistry, Cornell Un, Cornell University Press, Ithaca, N.Y., 1953.

[29] F. Khoury, E. Passaglia, The Morphology of Crystalline Synthetic Polymers, Treatise Solid State Chem., (1976) 335–496.

[30] A. Keller, A note on single crystals in polymers: Evidence for a folded chain configuration, Philos. Mag. 2 (1957) 1171–1175.

[31] P.J. Flory, Theory of crystallization in copolymers, Trans. Faraday Soc. 51 (1955) 848.

[32] P.J. Flory, Thermodynamics of Crystallization in High Polymers. I. Crystallization Induced by Stretching, J. Chem. Phys. 15 (1947) 397–408.

[33] V. DL, N. MR, R.G. Alamo, L. Mandelkern, Crystallization of PP, Polym Prep. 82 (2000) 140–142.

[34] D.W. van der Meer, J. Varga, G.J. Vancso, The influence of chain defects on the crystallisation behaviour of isotactic polypropylene, Express Polym. Lett. 9 (2015) 233–254.

[35] V. Busico, Giulio Natta and the Development of Stereoselective Propene Polymerization, in: Polyolefins 50 Years after Ziegler Natta I, Springer, (2013) 37–57.

[36] J.R. Severn, J.C. Chadwick, Tailor-Made Polymers, Wiley-VCH Verlag GmbH & Co. KGaA, Weinheim, Germany, 2008.

[37] S.Z.D. Cheng, J.J. Janimak, A. Zhang, E.T. Hsieh, Isotacticity effect on crystallization and melting in polypropylene fractions: 1. Crystalline structures and thermodynamic property changes, Polymer. 32 (1991) 648–655.

[38] C. Ruiz-orta, J.P. Fernandez-blazquez, A.M. Anderson-wile, G.W. Coates, R.G. Alamo, Isotactic Polypropylene with (3 , 1) Chain-Walking Defects : Characterization , Crystallization , and Melting Behaviors, Macromolecules. 44 (2011) 3436–3451.

[39] B. Crist, P.R. Howard, Crystallization and melting of model ethylene-butene copolymers, Macromolecules. (1999).

[40] G. Allegra, R.H. Marchessault, S. Bloembergen, Crystallization of markoffian copolymers, J. Polym. Sci. Part B Polym. Phys. 30 (1992) 809–815.

[41] S. Hosoda, Y. Nozue, Y. Kawashima, K. Suita, S. Seno, T. Nagamatsu, K.B. Wagener, B. Inci, F. Zuluaga, G. Rojas, Effect of the Sequence Length Distribution on the Lamellar Crystal Thickness and Thickness Distribution of Polyethylene: Perfectly Equisequential ADMET Polyethylene vs Ethylene/α-Olefin Copolymer., Macromolecules. 44 (2010) 313–319.

[42] E.G. and T. RP, Polymeric Materials: Structure, Properties, and Applications, 2001.

[43] Meer DW, Polymeric Materials: Structure, Properties, and Applications, The Netherlands, 2003.

[44] D.W. Meer, J. Varga, G.J. Vancso, The influence of chain defects on the crystallization behaviour of isotactic polypropylene, Express Polym. Lett. 9 (2015) 233–254.

[45] J.R. Severn, J.C. Chadwick, Tailor-made polymers: via immobilization of alpha-olefin polymerization catalysts, John Wiley & Sons, 2008.

[46] S.Z.D. Cheng, J.J. Janimak, A. Zhang, E.T. Hsieh, Isotacticity effect on crystallization and melting in polypropylene fractions: 1. Crystalline structures and thermodynamic property changes, Polymer (Guildf). 32 (1991) 648–655.

[47] P.J. Flory, Thermodynamics of crystallization in high polymers. IV. A theory of crystalline states and fusion in polymers, copolymers, and their mixtures with diluents, J. Chem. Phys. 17 (1949) 223–240.

[48] F. Chen, R.A. Shanks, G. Amarasinghe, Molecular distribution analysis of melt-crystallized ethylene copolymers, Polym. Int. 53 (2004) 1795–1805.

[49] L. Feng, M.R. Kamal, Distributions of Crystal Size from DSC Melting Traces for Polyethylenes, Can. J. Chem. Eng. 82 (2004) 1239–1251.

[50] M.R. Kamal, L. Feng, T. Huang, A Generalized Equation for the Prediction of Melting Temperatures of Homopolymers and Copolymers, Can. J. Chem. Eng. 80 (2002) 432–442.

[51] A.R. and M.L. Vanderhart DL, Nyden MR, Solid-state NMR investigation of paramagnetic nylon-6 clay nanocomposites. 1. Crystallinity, morphology, and the direct influence of Fe^{3+} on nuclear spins, Polym Prep. 82 (2001) 140–142.

[52] M. Atiqullah, S. Anantawaraskul, A.-H.M. Emwas, M.A. Al-Harthi, I. Hussain, A. Ul-Hamid, A. Hossaen, Effects of Supported (n BuCp)$_2$ ZrCl$_2$ Catalyst Active-Center Distribution on Ethylene–1-Hexene Copolymer Backbone Heterogeneity and Thermal Behaviors, Ind. Eng. Chem. Res. 52 (2013) 9359–9373.

[53] G.D. Wignall, R.G. Alamo, J.D. Londono, L. Mandelkern, M.H. Kim, J.S. Lin, G.M. Brown, Morphology of blends of linear and short-chain branched polyethylenes in the solid state by small-angle neutron and X-ray scattering, differential scanning calorimetry, and transmission electron microscopy, Macromolecules. 33 (2000) 551–561.

[54] M. Atiqullah, M.S. Winston, J.E. Bercaw, I. Hussain, A. Fazal, M.A. Al-Harthi, A.-H. Emwas, M.J. Khan, A. Hossaen, Effects of a vanadium post-metallocene catalyst-induced polymer backbone inhomogeneity on UV oxidative degradation of the resulting polyethylene film, Polym. Degrad. Stab. 97 (2012) 1164–1177.

[55] M. Atiqullah, M.A. Al-Harthi, S. Anantawaraskul, A.-H.M. Emwas, Ethylene homo-and copolymerization chain-transfers: A perspective from supported (n BuCp)$_2$ ZrCl$_2$ catalyst active centre distribution, J. Chem. Sci. 127 (2015) 717–728.

[56] T. Hayashi, Y. Inoue, R. Chûjô, T. Asakura, Heptad configurational analysis of ^{13}C NMR spectra in highly isotactic polypropylene, Polymer. 29 (1988) 138–143.

[57] B. Monrabal, P. del Hierro, Characterization of polypropylene–polyethylene blends by temperature rising elution and crystallization analysis fractionation, Anal. Bioanal. Chem. 399 (2011) 1557–1561.

[58] Y.H. Shi, Q. Dou, Non-isothermal crystallization kinetics of β-nucleated isotactic polypropylene, J. Therm. Anal. Calorim. 112 (2013) 901–911.

[59] S. Qin, J., Chen, X., Yu, J., Wang, Y., Tian, Y., & Wu, Nonisothermal Crystallization Kinetics of Isotactic Polypropylene Containing Nucleating Agent and Dispersant, J. Appl. Polym. Sci. 117 (2010) 1047–1054.

[60] L. Xu, X. Zhang, K. Xu, S. Lin, M. Chen, Variation of non-isothermal crystallization behavior of isotactic polypropylene with varying nucleating agent content, Polym. Int. 59 (2010) 1441–1450.

[61] S. Zhao, Z. Xin, Crystallization kinetics of isotactic polypropylene nucleated with organic dicarboxylic acid salts, J. Appl. Polym. Sci. 112 (2009) 1471–1480.

[62] M. Ghorbanzadeh Ahangari, A. Fereidoon, N. Kordani, H. Garmabi, Effect of nano-nucleating agent addition on the isothermal and nonisothermal crystallization kinetics of isotactic polypropylene, Polym. Bull. 66 (2011) 239–258.

[63] A. Fereidoon, M.G. Ahangari, S. Saedodin, Study of the Nonisothermal Crystallization Kinetics and Melting Behaviors of Polypropylene Reinforced with Single-Walled Carbon Nanotubes Nanocomposite, J. Macromol. Sci. Part B. 48 (2009) 25–40.

[64] S. Chin, S. Ai Tjong, Non-isothermal Crystallization Kinetics of Calcium Carbonate-filled b-Crystalline Phase Polypropylene Composites, Polym. Int. 95È103 Polym. Int. 44 (1997) 95–103.

[65] W. Xu, M. Ge, P. He, Nonisothermal crystallization kinetics of polypropylene/montmorillonite nanocomposites, J. Polym. Sci. Part B Polym. Phys. 40 (2002) 408–414.

[66] C. Grein, M. Gahleitner, B. Knogler, S. Nestelberger, Melt viscosity effects in ethylene–propylene copolymers, Rheol. Acta. 46 (2007) 1083–1089.

[67] S. Qiu, Y. Zheng, A. Zeng, Y. Guo, Prediction of non-isothermal crystallization parameters for isotactic polypropylene, Thermochim. Acta. 512 (2011) 28–33.

[68] A. Adhikari, K. Lozano, Effects of carbon nanofibers on the crystallization kinetics of polyethylene oxide, J. Polym. Res. 18 (2011) 875–880.

[69] D. Olmos, C. Domínguez, P.D. Castrillo, J. Gonzalez-Benito, Crystallization and final morphology of HDPE: Effect of the high energy ball milling and the presence of TiO_2 nanoparticles, Polymer. 50 (2009) 1732–1742.

[70] G.Z. Papageorgiou, D.S. Achilias, G.P. Karayannidis, Estimation of thermal transitions in poly(ethylene naphthalate): Experiments and modeling using isoconversional methods, Polymer. 51 (2010) 2565–2575.

[71] I. Acar, A. Durmu, S. Zgü, Nonisothermal Crystallization Kinetics and Morphology of Poly(ethylene terephthalate) Modified with Poly(lactic acid), J Appl Polym Sci. 106 (2007) 4180–4191.

[72] A. Gradys, P. Sajkiewicz, A.A. Minakov, S. Adamovsky, C. Schick, T. Hashimoto, K. Saijo, Crystallization of polypropylene at various cooling rates, Mater. Sci. Eng. A. 413 (2005) 442–446.

[73] A. Hammami, J.E. Spruiell, A.K. Mehrotra, Quiescent nonisothermal crystallization kinetics of isotactic polypropylenes, Polym. Eng. Sci. 35 (1995) 797–804.

[74] P. Supaphol, N. Dangseeyun, P. Srimoaon, M. Nithitanakul, Nonisothermal melt-crystallization kinetics for three linear aromatic polyesters, Thermochim. Acta. 406 (2003) 207–220.

[75] S.S. Sahay, K. Krishnan, Analysis of the nonisothermal crystallization kinetics in three linear aromatic polyester systems, Thermochim. Acta. 430 (2005) 23–29.

[76] H. Randall, Polymer sequence determination (the 13C method), (1977).

[77] R. Paukkeri, T. Väänänen, A. Lehtinen, Microstructural analysis of polypropylenes produced with heterogeneous Ziegler-Natta catalysts, Polymer. 34 (1993) 2488–2494.

[78] A.K. Galwey, What is meant by the term “variable activation energy” when applied in the kinetic analyses of solid state decompositions (crystolysis reactions)?, Thermochim. Acta. 397 (2003) 249–268.

[79] A.K. Galwey, Eradicating erroneous Arrhenius arithmetic, Thermochim. Acta. 399 (2003) 1–29.

[80] H. Eloussifi, J. Farjas, P. Roura, M. Dammak, Non-isothermal model-free predictions, J. Therm. Anal. Calorim. 108 (2012) 597–603.

[81] K. Chrissafis, K.M. Paraskevopoulos, S.Y. Stavrev, A. Docoslis, A. Vassiliou, D.N. Bikiaris, Characterization and thermal degradation mechanism of isotactic polypropylene/carbon black nanocomposites, Thermochim. Acta. 465 (2007) 6–17.

[82] Q. Zhou, A. Wang, H. Li, Z. Luo, T. Zheng, L. Zhang, Y. Hu, Microstructure of polypropylene and active center in Ziegler–Natta catalyst: effect of novel salicylate internal donor, RSC Adv. 6 (2016) 75023–75031.

[83] B. Crist, T.M. Finerman, Copolymer crystallization: Approaching equilibrium, Polymer (Guildf). 46 (2005) 8745–8751.

[84] R.G. Alamo, L. Mandelkern, The crystallization behavior of random copolymers of ethylene, Thermochim. Acta. 238 (1994) 155–201.

[85] R.G. Alamo, L. Mandelkern, Crystallization kinetics of random ethylene copolymers, Macromolecules. 24 (1991) 6480–6493.

[86] R. Alamo, R. Domszy, L. Mandelkern, Thermodynamic and structural properties of copolymers of ethylene, J. Phys. Chem. 88 (1984) 6587–6595.

[87] R.S. and K.A. Hikosaka M, Okada H, Toda A, Temperature window effect and its application in extrusion of ultrahigh molecular weight polyethylene, Chem Soc Faraday Trans. (1995) 2573–2579.

[88] M. Hikosaka, S. Rastogi, A. Keller, H. Kawabata, Investigations on the crystallization of polyethylene under high pressure: role of mobile phases, lamellar thickening growth, phase transformations, and morphology, J. Macromol. Sci. Part B Phys. 31 (1992) 87–131.

[89] S. Rastogi, M. Hikosaka, H. Kawabata, A. Keller, Role of mobile phases in the crystallization of polyethylene. Part 1. Metastability and lateral growth, Macromolecules. 24 (1991) 6384–6391.

[90] C.A. Avila-Orta, F.J. Medellín-Rodríguez, M. V. Dávila-Rodríguez, Y.A. Aguirre-Figueroa, K. Yoon, B.S. Hsiao, Morphological features and melting behavior of nanocomposites based on isotactic polypropylene and multiwalled carbon nanotubes, J. Appl. Polym. Sci. 106 (2007) 2640–2647.

[91] C.I. Ferreira, C. Dal Castel, M.A.S. Oviedo, R.S. Mauler, Isothermal and non-isothermal crystallization kinetics of polypropylene/exfoliated graphite nanocomposites, Thermochim. Acta. 553 (2013) 40–48.

[92] M. Razavi-Nouri, M. Ghorbanzadeh-Ahangari, A. Fereidoon, M. Jahanshahi, Effect of carbon nanotubes content on crystallization kinetics and morphology of polypropylene, Polym. Test. 28 (2009) 46–52.

[93] J.-Z. Xu, C. Chen, Y. Wang, H. Tang, Z.-M. Li, B.S. Hsiao, Graphene Nanosheets and Shear Flow Induced Crystallization in Isotactic Polypropylene Nanocomposites, Macromolecules. 44 (2011) 2808–2818.

[94] K. Kalaitzidou, H. Fukushima, P. Askeland, L.T. Drzal, The nucleating effect of exfoliated graphite nanoplatelets and their influence on the crystal structure and electrical conductivity of polypropylene nanocomposites, J Mater Sci. 43 (2008) 2895–1907.

[95] B. Yuan, C. Bao, L. Song, N. Hong, K.M. Liew, Y. Hu, Preparation of functionalized graphene oxide/polypropylene nanocomposite with significantly improved thermal stability and studies on the crystallization behavior and mechanical properties, Chem. Eng. J. 237 (2014) 411–420.

[96] A. Fereidoon, M.G. Ahangari, S. Saedodin, Study of the Nonisothermal Crystallization Kinetics and Melting Behaviors of Polypropylene Reinforced with Single-Walled Carbon Nanotubes Nanocomposite, J. Macromol. Sci. Part B. 48 (2009) 25–40.

[97] M. Ghorbanzadeh Ahangari, B.A. Fereidoon, B.N. Kordani, B.H. Garmabi, Á.A. Fereidoon Á N Kordani, H. Garmabi, Effect of nano-nucleating agent addition on the isothermal and nonisothermal crystallization kinetics of isotactic polypropylene, Polym. Bull. 66 (2011) 239–258.

[98] E. Assouline, A. Lustiger, A.H. Barber, C.A. Cooper, E. Klein, E. Wachtel, H.D. Wagner, Nucleation Ability of Multiwall Carbon Nanotubes in Polypropylene Composites, J Polym Sci Part B Polym Phys. 41 (2003) 520–527.

[99] T. Kuilla, S. Bhadra, D. Yao, N.H. Kim, S. Bose, J.H. Lee, Recent advances in graphene based polymer composites, Prog. Polym. Sci. 35 (2010) 1350–1375.

[100] S.R. Ahmad, C. Xue, R.J. Young, The mechanisms of reinforcement of polypropylene by graphene nanoplatelets, Mater. Sci. Eng. B Solid-State Mater. Adv. Technol. (2016).

[101] S. V. Polschikov, P.M. Nedorezova, A.N. Klyamkina, A.A. Kovalchuk, A.M. Aladyshev, A.N. Shchegolikhin, V.G. Shevchenko, V.E. Muradyan, Composite materials of graphene nanoplatelets and polypropylene, prepared by in situ polymerization, J. Appl. Polym. Sci. 127 (2013) 904–911.

[102] K. Gaska, X. Xu, S. Gubanski, R. Kádár, Electrical, Mechanical, and Thermal Properties of LDPE Graphene Nanoplatelets Composites Produced by Means of Melt Extrusion Process, Polymers. 9 (2017) 11.

[103] B. Kalantari, M.R.M. Mojtahedi, F. Sharif, R.S. Rahbar, Effect of graphene nanoplatelets presence on the morphology, structure, and thermal properties of polypropylene in fiber melt-spinning process, Polym. Compos. 36 (2015) 367–375.

[104] Y. Li, J. Zhu, S. Wei, J. Ryu, L. Sun, Z. Guo, Poly(propylene)/graphene nanoplatelet nanocomposites: Melt rheological behavior and thermal, electrical, and electronic properties, Macromol. Chem. Phys. 212 (2011) 1951–1959.

[105] M. El Achaby, F.-E. Arrakhiz, S. Vaudreuil, A. el Kacem Qaiss, M. Bousmina, O. Fassi-Fehri, Mechanical, thermal, and rheological properties of graphene-based polypropylene nanocomposites prepared by melt mixing, Polym. Compos. 33 (2012) 733–744.

[106] M. Van Drongelen, T.B. Van Erp, G.W.M. Peters, Quantification of non-isothermal, multi-phase crystallization of isotactic polypropylene: the influence of cooling rate and pressure, Polymer. 53 (2012) 4758–4769.

[107] M.L. Di Lorenzo, C. Silvestre, Non-isothermal crystallization of polymers, Prog. Polym. Sci. 24 (1999) 917–950.

[108] C.C. Hsu, P.H. Geil, H. Miyaji, K. Asai, Structure and properties of polypropylene crystallized from the glassy state, J. Polym. Sci. Part B Polym. Phys. 24 (1986) 2379–2401.

[109] A.P. Bafana, X. Yan, X. Wei, M. Patel, Z. Guo, S. Wei, E.K. Wujcik, Polypropylene nanocomposites reinforced with low weight percent graphene nanoplatelets, Compos. Part B Eng. 109 (2017) 101–107.

[110] S.C. Tjong, S.A. Xu, Non-isothermal crystallization kinetics of calcium carbonate-filled β-crystalline phase polypropylene composites, Polym. Int. 44 (1997) 95–103.

[111] J. Qin, X. Chen, J. Yu, Y. Wang, Y. Tian, S. Wu, Nonisothermal crystallization kinetics of isotactic polypropylene containing nucleating agent and dispersant, J. Appl. Polym. Sci. 117 (2010) 1047–1054.

[112] L. Xu, X. Zhang, K. Xu, S. Lin, M. Chen, Variation of non-isothermal crystallization behavior of isotactic polypropylene with varying β-nucleating agent content, Polym. Int. 59 (2010) 1441–1450.

[113] S. Zhao, Z. Xin, Crystallization kinetics of isotactic polypropylene nucleated with organic dicarboxylic acid salts, J. Appl. Polym. Sci. 112 (2009) 1471–1480.

[114] M. Atiqullah, M.M. Hossain, M.S. Kamal, M.A. Al-Harthi, M.J. Khan, A. Hossaen, I. Hussain, Crystallization Kinetics of PE-b-isotactic PMMA Diblock Copolymer Synthesized Using $SiMe_2$ $(Ind)_2$ $ZrMe_2$ and MAO Cocatalyst, AIChE J. 59 (2013) 200–214.

[115] P.J. Flory, Theory of crystallization in copolymers, Trans. Faraday Soc. 51 (1955) 848–857.

[116] B. Crist, P.R. Howard, Crystallization and melting of model ethylene-butene copolymers, Macromolecules. 32 (1999) 3057–3067.

[117] P.J. Flory, Thermodynamics of crystallization in high polymers. IV. A theory of crystalline states and fusion in polymers, copolymers, and their mixtures with diluents, J. Chem. Phys. 17 (1949) 223–240.

[118] M. Atiqullah, S. Adamu, M.M. Hossain, M.A. Al-Harthi, S. Anantawaraskul, A. Hossaen, Effects of supported (n $BuCp)_2$ $ZrCl_2$ catalyst active center multiplicity on crystallization kinetics of ethylene homo-and copolymers, J. Taiwan Inst. Chem. Eng. 45 (2014) 1982–1991.

[119] M. Atiqullah, M.M. Hossain, S. Adamu, A. Hossaen, Thermal behaviour of polyethylene-block-poly(methyl methacrylate) block copolymer: Effect of multiple heating and cooling rates versus mathematical artefact, Polym. Int. 63 (2014) 1824–1834.

[120] A. Adhikari, K. Lozano, Effects of carbon nanofibers on the crystallization kinetics of polyethylene oxide, J. Polym. Res. (2011).

[121] I. Acar, A. Durmuş, S. Özgümüş, Nonisothermal crystallization kinetics and morphology of poly (ethylene terephthalate) modified with poly (lactic acid), J. Appl. Polym. Sci. 106 (2007) 4180–4191.

[122] K.A. Jackson, Kinetic Processes: Crystal Growth, Diffusion, and Phase Transformations in Materials, John Wiley & Sons, 2006.

[123] M. Hikosaka, H. Okada, A. Toda, S. Rastogi, A. Keller, Dependence of the lamellar thickness of an extended-chain single crystal of polyethylene on the degree of supercooling and the pressure, J. Chem. Soc. Faraday Trans. 91 (1995) 2573–2579.

Vitae

Name: Abdullah Khaleel Ahmed

Nationality: Indian

Date of birth: May 12, 1990

Email: abdulcolor@gmail.com
abdullahkhaleel90@outlook.com
g201404500@kfupm.edu.sa

Current address: Room 224, Building 814, Student housing, King Fahd University of Petroleum & Minerals, Dhahran, Saudi Arabia

Permanent address: Sr. No: 24/2, Plot No: 41, Tashqand Bag, Malegaon, Nashik, Maharashtra, India

Academic background: BS Chemical Engineering from Savitribai Pule Pune University, 2012
MS Chemical Engineering from King Fahd University of Petroleum & Minerals, 2017